

Non-stationary time series attribution for heatwaves over Europe

Pascal Meurer, Sebastian Buschow, Svenja Szemkus, and Petra Friederichs

Institute of Geosciences, University of Bonn

Auf dem Hügel 20, 53121 Bonn, Germany

Correspondence: Pascal Meurer (pmeurer@uni-bonn.de) and Petra Friederichs (pfried@uni-bonn.de)

Abstract.

The increasing occurrence of extreme weather events since the beginning of the 21st century has led to the development of new methods to attribute extreme events to anthropogenic climate change. How the extreme event is defined has a major influence on the attribution result. A frequently disregarded or evaded aspect concerns the temporal dependence and the clustering of extremes. This study presents an approach for attributing complete time series during extreme events to anthropogenic forcing. The approach is based on a non-stationary Markov process using bivariate extreme value theory to model the temporal dependence of the time series. We calculate the likelihood ratio of an observational time series from ERA5 given the distributions as estimated from CMIP6 simulations with historical natural-only and natural and anthropogenic forcing scenarios. The spatial fields are condensed by the extremal pattern index as a compact description of spatial extremes. In addition, the study examines the extent to which attribution statements about the occurrence of extreme heat events change when the effect of the mean warming is eliminated. The resulting attribution statement provides very strong evidence for the scenario with anthropogenic drivers over Europe, especially since the beginning of the 21st century. For central and southern Europe, the influence of anthropogenic greenhouse gas emissions on heatwaves could already have been proven in the 1970s using today's methods. There is no reliable signal apart from a general increase in temperature, neither in terms of the temporal dependence of extreme heat days nor in terms of the shape of the extreme value distribution.

Copyright statement. TEXT

1 Introduction

The consequence of the considerable increase in greenhouse gases resulting from the extensive use of fossil energy sources by humans, coupled with the substantial alterations in land use, has led to the emergence of an ongoing global climate change phenomenon, which began approximately a century ago (Gulev et al., 2021). In recent years, annual greenhouse gas emissions have reached unprecedented levels (IEA, 2021). This trend is mirrored by the concentration of CO_2 , CH_4 and N_2 gases, which have reached levels that have not been seen for at least 800,000 years (Gulev et al., 2021). The Earth's climate system is undergoing a transformation as a consequence of alterations in atmospheric decomposition. To investigate these changes in the

climate system, in the 1980s and 1990s the focus of scientific interest was on detecting the changes in climate that had been observed (e.g., the increase in global mean temperature). These detection studies have already demonstrated the strong signal of anthropogenic climate change in observed changes in global mean surface temperature (Hegerl et al., 2006).

In addition to the increase in global mean temperature, the occurrence of extreme events such as heatwaves has increased since the beginning of the 21st century. This has led to a growing number of studies on the attribution of extreme weather events (Hulme, 2014; Seneviratne et al., 2021). One of the first studies of this kind was conducted by Stott et al. (2004). The studies aim to investigate whether changes in extreme weather can be attributed to anthropogenic climate change. Several methods for the attribution of extreme events have been established that focus the attribution statement on a single extreme event, such as a heatwave or flood event (Perkins-Kirkpatrick et al., 2024). Typically, a data compression method (e.g., moving average over a region) is used to attribute the event based on univariate extreme value statistics (Philip et al., 2020). The attribution is then performed by calculating the probability of the event given factual and counterfactual conditions, based on the so-called causal counterfactual theory (Hannart et al., 2016). These probabilities are then compared using a probability ratio, or in the case of a time series the likelihood ratio (Seong et al., 2022).

The temporal evolution and dependence is often ignored, or techniques are used to break down the time series into individual clusters of extreme values (Philip et al., 2020; Sippel et al., 2015; Wehner et al., 2016). A useful extension in extreme value statistics is the modelling of temporal dependence for extreme events (Fawcett and Walshaw, 2006). We use this approach to include temporal dependence in the attribution approach. The question of attribution for periods without extreme events is also relevant. For example, one may consider the attribution of a summer with cold spells and heat extremes. The European summer of 2025, for example, included cold spells as well as heat extremes (see Sect. 2.2.1). In this study, we present an approach for attributing complete time series that consist of extreme and non-extreme events. This allows us to extend the attribution not only to entire summer periods, but also to a series of summers. One can then assess whether non-extreme parts of the time series contribute to evidence for the greenhouse gas scenario, and if not, how strong the opposing evidence is. In this sense, the likelihood ratio can be updated by adding additional observations to the attribution.

Since we want to process data with spatial and temporal dimensions and obtain reliable probabilities for extreme events, the first step is to reduce the dimensions in space using a suitable data compression method. We use a method presented by Szemkus and Friederichs (2024) based on a decomposition of extremal dependency. Their approach is closely related to principal component analysis, as used, for example, to identify teleconnections in the atmosphere, and follows Cooley and Thibaud (2019) and Jiang et al. (2020). Instead of correlation or covariance, a measure specifically designed for the dependence of extremes is used to identify spatially coherent patterns. The extremal pattern index (EPI) as introduced in Szemkus and Friederichs (2024) then provides a spatially aggregated measure of the strength of an extremal pattern of a meteorological variable.

The temporal dependence of the daily EPI time series is considered by using a Markov process. The Markov process can be described by an approximate likelihood based on bivariate extreme value theory (Smith et al., 1997; Beirlant et al., 2004). This likelihood is based on the censored likelihood model, which divides the two-dimensional plane into four regions according to whether or not the variables exceed the threshold value. The corresponding two-dimensional variable represents two con-

secutive observations in the Markov process. The resulting dependency is thus analogous to autocorrelation in a time series. Declustering the extremes in a time series is therefore no longer necessary. The approach is applied to different scenarios, represented by an ensemble of CMIP6 simulations, so that we can compare the likelihood of an observational time series given different scenarios. For each scenario, a set of model parameters can be estimated, and an attribution statement can be made by the respective likelihood ratio.

This study examines heatwaves, which are described by the maximum daily temperature near the surface. We would like to answer the following questions in particular.

1. Can the temporal evolution of a heatwave be attributed to anthropogenic emissions?
2. Are the extremes becoming more extreme, i.e., is there a climate change signal beyond a general warming?

For both questions, we adapt the Markov process model further to account for non-stationary conditions and ongoing changes in the climate system, following Hannart et al. (2016). They pointed out that the stationarity assumption is unrealistic because mean temperature and thus extremes changed over time. Based on slow-varying covariates, possible changes in the parameters can be modelled.

The article is structured as follows. Section 2 introduces the data used in this study, as well as the compact description of multivariate weather events in terms of EPI. The daily maximum surface temperatures in Europe in the summer of 2025 are used to illustrate the methods. In Sect. 3 we briefly introduce the attribution approach for extreme events, present the derivation of the approximate likelihood for the Markov process, and introduce non-stationarity. In Sect. 4, the workflow for the attribution using the Markov process model is presented. In Sect. 5, the results for heatwaves are presented. Lastly, Sect. 6 discusses these results and gives our concluding remarks.

2 Data and Indices

2.1 Data

We used the daily maximum 2 meter temperature (T2max) of the ERA5 reanalysis (Hersbach et al., 2020) in Europe. ERA5 provides a spatially and temporally consistent description of the atmospheric state since 1940 based on data assimilation. We focus our study on daily time series during the northern hemispheric summer seasons June to August (JJA).

Historic simulations are taken from the CMIP6 and DAMIP v1.0 projects (Gillett et al., 2016). The scenarios we use are historical-natural (HIST-NAT) without anthropogenic forcing, historical scenario (HIST) and SPP2-4.5 with anthropogenic forcing. The respective circulation model, the variable, and the number of members available in the ensemble are given in Table 1. As for the ERA5 dataset, we focus on JJA-months. The study area consists of only land points. A grid cell is considered a land point when at least 50% of the cell is occupied by land. We used the AR6 regions shown in Fig. 1 of northern, central and southern Europe (Iturbide et al., 2020). The regions in North Africa are excluded from the analysis due to their different climates with extremely dry desert areas.

Table 1. Number and type of CMIP6 simulations with HIST (1940-2014), SPP2-4.5 (2015-2025), and HIST-NAT (1940-2020) for T2max used in this study.

Number and type of CMIP6 simulations			
Variable Scenario	T2max HIST	T2max SPP2-4.5	T2max HIST-NAT
access-esm1-5	19	18	3
bcc-csm2-mr	3	1	3
canesm5	50	50	10
cnrm-cm6-1	30	1	3
hadgem3	4	4	4
ipsl-cm6a-lr	32	11	6
miroc6	50	49	50
mri-esm2-0	7	4	5
mpi-esm1-2-lr	50	50	30

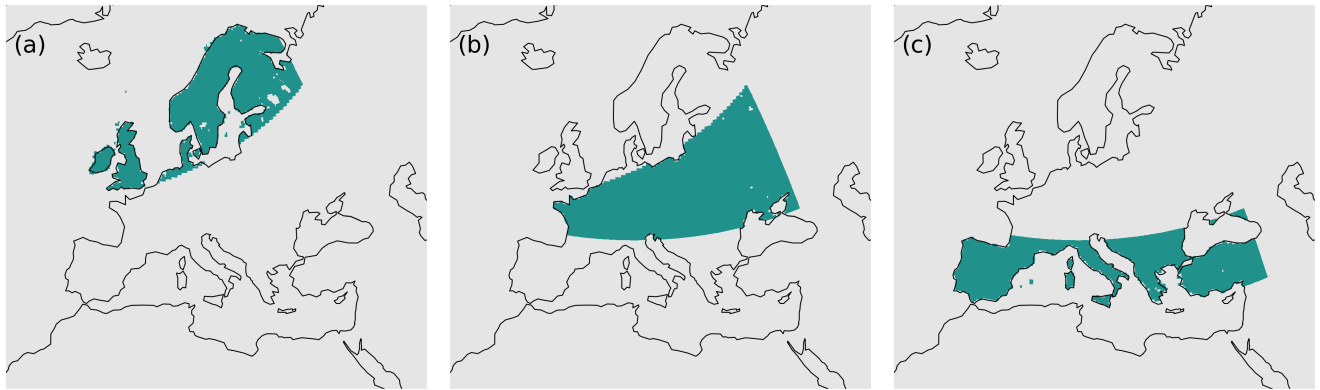


Figure 1. AR6 regions (Iturbide et al., 2020) of (a) northern, (b) central, and (c) southern Europe as used in this study with North Africa excluded and restricted to land points only. A grid cell is considered as land point when at least 50% of the cell is occupied by land.

2.2 Extremal pattern index (EPI)

Our compact representation of a spatially extended multivariate weather event uses the EPI as suggested in Szemkus and Friederichs (2024). The approach is based on the decomposition of high-dimensional data based on a description of the tail dependence within the framework of regular variation (Cooley and Thibaud, 2019). The reader is referred to Szemkus and Friederichs (2024) for the details of the method.

We consider a data set containing daily values. The annual cycle is initially removed from the daily data set during JJA. For this purpose, the T2max values for each day of the JJA period and grid point are standardized using the respective mean value and standard deviation. Subsequently, the data at each grid point are transformed to a standard distribution. In our case, this is a α -Fréchet distribution with $\alpha = 2$. The pairwise measure of dependence between extreme events at two locations is calculated for each pair of land grid points in Europe. In order to capture only the dependence for extreme events, we select only those points in time at which the transformed variable lies in the top 1% range of the respective distribution at both locations. The result is a matrix of extremal dependencies, referred to as the tail pairwise dependence matrix (TPDM), with dimensions $q \times q$, where q is the number of land grid points. The eigenvectors of the TPDM represent spatial variation patterns, indicating regions where extremes occur together with greater frequency.

The eigenvalues $\lambda_j, j = 1, \dots, q$ are indicative of the proportion of the pattern j within the total variability of the standardised extreme events. The projection of the j -th pattern onto the standardised data results in a time series $\eta_j(t)$, denoted as principal components (PCs). They represent the strength of the pattern j at time t . The total variability of the first ten variation patterns is summarised in the extremal pattern index (EPI, Szemkus and Friederichs, 2024). The EPI is defined as

$$\text{EPI}_t^\eta = \frac{\sqrt{\sum_{k=1}^m \eta_{t,k}^2}}{\sqrt{\sum_{j=1}^m \lambda_j}} \quad (1)$$

with $\lambda_{1,\dots,m}$ and the leading m eigenvalues and represents a spatial aggregation of the extremal state of the variable in space (Szemkus and Friederichs, 2024). Normalisation within the definition of the EPI with the sum of the eigenvalues in Eq. (1) enables comparison between data sets that exhibit different levels of variability. This is the case, for example, when the data represent different regions or are available on different spatial grids.

With the help of the EPI, multivariate extreme events that have a spatial extent can be described by a univariate index that has only a temporal dimension and takes into account dependencies in space at extreme levels. In this study, the method is applied to different AR6 regions (Fig. 1), i.e., the TPDM is calculated and decomposed separately for each region.

2.2.1 Example: Summer 2025 in Europe

The European summer of 2025 was characterised by a series of heatwave events across Europe. An early heatwave began in southwestern Europe in June and the highest average surface air temperatures between 17 June and 2 July 2025 compared to the period 1979-2024 were recorded in the Iberian Peninsula, large parts of France extending to Germany and southern Great Britain as reported in Copernicus Climate Change Service (2025). Figure 2 shows the EPI for the regions in Fig. 1 and the T2max anomalies for summer 2025 over Europe. The early onset of the remarkable heatwave over southwestern Europe is visible at the end of the first week of June (Fig. 2). This event lasted until the beginning of July. As is common in this region, this heatwave was mainly caused by atmospheric ridges, as evident from the large-scale circulation pattern during the heatwave (not shown here, Faranda et al. (2025)). Regarding the spatial extent, most parts of the southern and central European regions except Turkey were influenced by this event. Two additional strong heatwave events have been observed in southern Europe, one in the second half of July and one in the first half of August. The event in July occurred over the

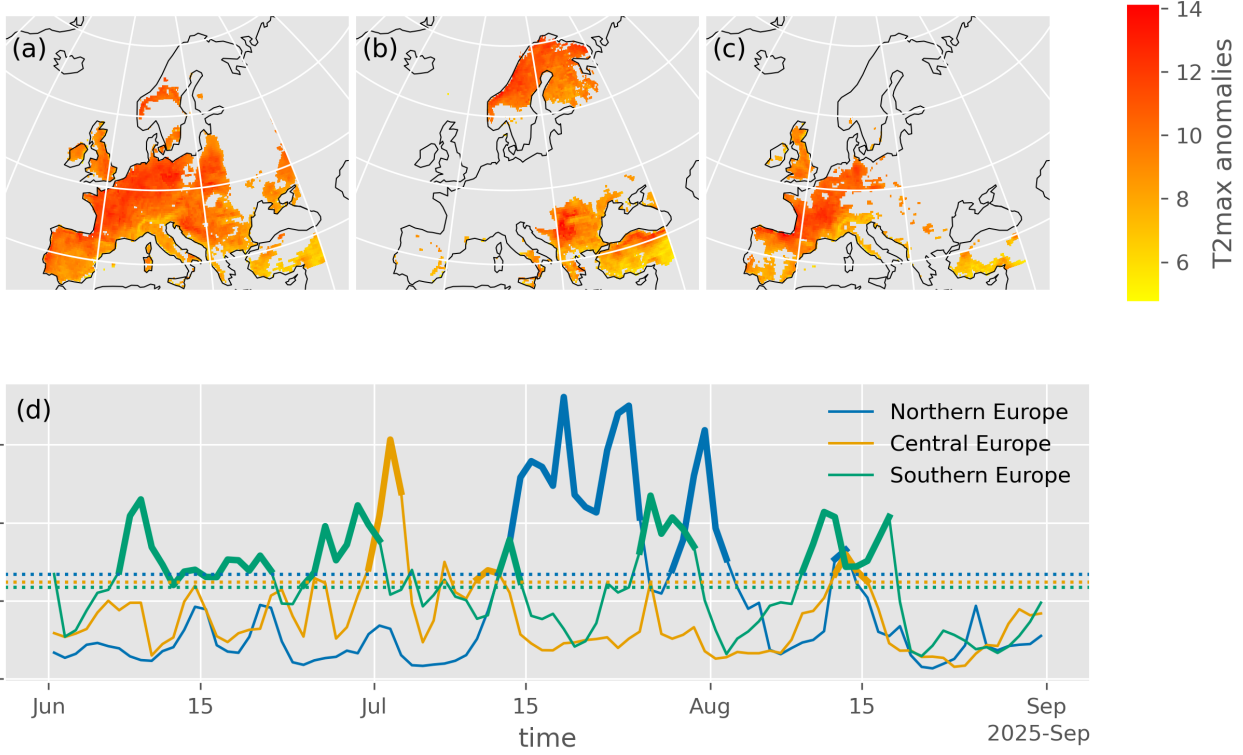


Figure 2. Mean T2max anomalies in ERA5 between (a) 07 June to 5 July 2025, (b) 15 July to 01 August 2025, and (c) 07 August to 19 August 2025. Only grid points exceeding the 99%-quantile are shown. In (d) the EPI for T2max from June to August 2025 for northern (blue), central (orange) and southern (green) European regions from Fig. 1 is shown. The EPI is bold if it exceeds the corresponding 95% quantile (1940-2025) of the region, whereby the quantile is indicated as dotted line.

eastern Mediterranean, whereas the event in August took place over the western Mediterranean, affecting Spain, Portugal, and France. Another remarkable heatwave in 2025 occurred over Scandinavia, approximately mid-July to early August. This event received large media attention, and was investigated by the world weather attribution in a report (Barnes et al., 2025). A detailed description of the synoptic situation and the resulting temperature extremes can be found in the report.

3 Theory and Methods

3.1 Attribution of extreme events

The attribution of extreme events corresponds to the statistical answer to the question of whether or not a specific event was caused by anthropogenic climate change. The theoretical foundation of the attribution is presented in detail by Hannart and Naveau (2018) and is based on the so-called causal counterfactual theory. Defining the scenario with climate change as m_1 and

the scenario without climate change as m_0 , the main result of the attribution is given by the probability of necessity, which is defined as

$$\text{PN} = \mathbb{P}(\neg X | \text{do}(m_0), m_1, X). \quad (2)$$

This describes the probability that the event X would not have occurred (denoted $\neg X$) in the absence of m_1 , denoted by $\text{do}(m_0)$ (i.e., experimentally enforcing the scenario to be m_0), given that both the event X and the scenario m_1 have, in fact, occurred. Under certain conditions mentioned by Hannart and Naveau (2018), PN can be formulated as

$$\text{PN} = 1 - \frac{p_0}{p_1}, \quad (3)$$

with p_0 as the probability of an event given a scenario without anthropogenic emissions (HIST-NAT) and p_1 as the probability of the same event given a scenario with anthropogenic emissions (HIST). This term is equivalent to the fraction of attributable risk (FAR) often used in attribution studies (Perkins-Kirkpatrick et al., 2024). If $\text{PN} > 0$, anthropogenic climate change contributed to the event or, in other words, made it more likely to occur. It is also common to rewrite $\text{PN} > 0$ in terms of the probability ratio PR defined as

$$\text{PR} = \frac{p_1}{p_0}, \quad (4)$$

such that $\text{PN} = 1 - 1/\text{PR}$.

In this study, we are interested in the probability of a time series $\mathbf{d} = (d_1, \dots, d_T)$, e.g., the evolution of the daily EPI as given by ERA5, given different scenarios, in our case m_0 (HIST-NAT) and m_1 (HIST). The probability ratio then becomes a likelihood ratio (LR)

$$\text{LR}(\mathbf{d}) = \frac{l(\mathbf{d}|m_1)}{l(\mathbf{d}|m_0)}, \quad (5)$$

with $l(\mathbf{d}|m_i)$ the likelihood of observing a given time series \mathbf{d} in the scenario m_i .

From a Bayesian point of view, attribution could be stated as the ratio of the posterior odds for the scenarios (Kass and Raftery, 1995) using all data $(\mathbf{d}^{(1)}, \dots, \mathbf{d}^{(n)})$, with n indicating the most recent year, given as

$$\frac{\mathbb{P}(m_1 | \mathbf{d}^{(n)}, \dots, \mathbf{d}^{(1)})}{\mathbb{P}(m_0 | \mathbf{d}^{(n)}, \dots, \mathbf{d}^{(1)})} = \frac{l(\mathbf{d}^{(n)} | m_1, \mathbf{d}^{(n-1)}, \dots, \mathbf{d}^{(1)}) \mathbb{P}(m_1 | \mathbf{d}^{(n-1)}, \dots, \mathbf{d}^{(1)})}{l(\mathbf{d}^{(n)} | m_0, \mathbf{d}^{(n-1)}, \dots, \mathbf{d}^{(1)}) \mathbb{P}(m_0 | \mathbf{d}^{(n-1)}, \dots, \mathbf{d}^{(1)})}. \quad (6)$$

We now assume that the daily time series during one season are conditionally independent of the daily time series during the same season the year before or after. In case of conditional independence $l(\mathbf{d}^{(n)} | m_0, \mathbf{d}^{(n-1)}, \dots, \mathbf{d}^{(1)}) = l(\mathbf{d}^{(n)} | m_0)$, Eq. (6) can be reformulated as

$$\frac{\mathbb{P}(m_1 | \mathbf{d}^{(n)}, \dots, \mathbf{d}^{(1)})}{\mathbb{P}(m_0 | \mathbf{d}^{(n)}, \dots, \mathbf{d}^{(1)})} = \underbrace{\frac{l(\mathbf{d}^{(n)} | m_1)}{l(\mathbf{d}^{(n)} | m_0)}}_{\text{LR}(\mathbf{d}^{(n)})} \frac{\mathbb{P}(m_1 | \mathbf{d}^{(n-1)}, \dots, \mathbf{d}^{(1)})}{\mathbb{P}(m_0 | \mathbf{d}^{(n-1)}, \dots, \mathbf{d}^{(1)})} = \prod_{i=1}^n \text{LR}(\mathbf{d}^{(i)}) \frac{\mathbb{P}(m_1)}{\mathbb{P}(m_0)}. \quad (7)$$

The likelihood ratio $\text{LR}(\mathbf{d}^{(i)}) = l(\mathbf{d}^{(i)} | m_1) / l(\mathbf{d}^{(i)} | m_0)$ then represents the additional evidence that an event $\mathbf{d}^{(i)}$ adds to the total evidence. The posterior ratio is equivalent to the product of the likelihood ratios in the case of uniform prior probabilities.

The product of the probability ratios in Eq. (7) corresponds to the Bayes factor. If we now vary the most recent analysis year n from 1940 to 2025, we can assess when in the past we would have had sufficient evidence of climate change with the means available to us today. A statement on evidence based on the Bayes factor is given in Table 2, which differs slightly from the one given in Kass and Raftery (1995). Given that interpretation is context dependent, Table 2 provides a general indication of the level of evidence.

Table 2. Scales of the likelihood ratio and related evidence as given in Seong et al. (2022).

log LR	LR	Evidence against p_0
0-1	1-3	Not worth more than a bare mention
1-2.5	3-12	Substantial
2.5-5	12-150	Strong
> 5	> 150	Decisive

3.2 Likelihood formulation

The likelihood of a time series \mathbf{d} modelled by a first-order Markov process is given by

$$l(\mathbf{d}; \boldsymbol{\theta}) = l(d_1, \dots, d_n; \boldsymbol{\theta}) = l(d_1; \boldsymbol{\theta}_1) \prod_{i=2}^n l(d_i | d_{i-1}; \boldsymbol{\theta}_1, \boldsymbol{\theta}_2) = \frac{\prod_{i=2}^n l(d_{i-1}, d_i; \boldsymbol{\theta}_1, \boldsymbol{\theta}_2)}{\prod_{i=2}^{n-1} l(d_i; \boldsymbol{\theta}_1)}, \quad (8)$$

where $\boldsymbol{\theta} = (\boldsymbol{\theta}_1, \boldsymbol{\theta}_2)$ denotes the complete parameter vector, $\boldsymbol{\theta}_1$ contains the parameters of the marginal distributions, and $\boldsymbol{\theta}_2$ the dependence parameters. Due to the first-order Markov assumption, the state of time i depends only on the state of time $i-1$, and thus the dependence structure in $l(d_{i-1}, d_i; \boldsymbol{\theta}_1, \boldsymbol{\theta}_2)$ can be decomposed using pairwise likelihoods. Since we are interested in the extremes of the Markov process, a bivariate extreme value theory is required to develop an approximate probability formulation (see Sect. 10.4 in Beirlant et al. (2004)). Here, we are only interested in the behaviour of the process above a high threshold (Smith et al., 1997, Sect. 1).

For a stationary Markov process $\{D_n\}_{n \geq 1}$, we consider a bivariate random variable (D_1, D_2) with joint distribution $F(d_1, d_2)$, joint density function $f(d_1, d_2)$, and the marginal density function of the Markov process with $f(d)$. For the extremes, we assume that $F(d_1, d_2)$ lies in the domain of attraction of $G(d_1, d_2)$ ($F \in \mathcal{D}(G)$), which must be a bivariate extreme value distribution. In particular, we can write

$$F(d_1, d_2) \approx \exp\{-l^*(v_1, v_2, \theta)\} \quad (9)$$

for $d_i > u_i$ ($i = 1, 2$) and u_i as a sufficiently high threshold value and l^* as the tail-dependence function, whereby

$$1/v_j = \phi_j^{-1} \left(1 + \xi_j \frac{d_j - u_j}{\sigma_j} \right)^{\frac{1}{\xi_j}} \quad (10)$$

with ϕ_j as the probability of the exceedance over a threshold u_j , ξ_j as the shape parameter and σ_j as the scale parameter. For the margins, we assume that $F_j(d_j) \approx \exp\{-v_j\} \sim \text{GPD}$. Then it remains to specify a parametric form of l^* .

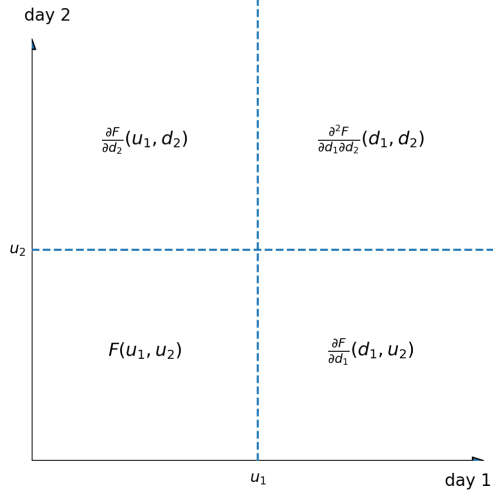


Figure 3. Regions of the censored likelihood model according to Eq. (12), whereby the likelihood contribution depends on which variable is exceeding the threshold or not.

Often, l^* is modelled using a parametric family. A common choice is the logistic model with

$$l^*(v_1, v_2) = \left(v_1^{1/\alpha} + v_2^{1/\alpha} \right)^\alpha, \quad v_j \geq 0. \quad (11)$$

The dependence parameter $0 < \alpha \leq 1$ represents independence if $\alpha = 1$ and complete dependence if $\alpha \rightarrow 0$. It is important to note that this model cannot capture asymptotic independence, which is a property that holds for all max-stable models (Huser et al., 2021, Sect. 2.3). For a different choice of the stable tail dependence function $l^*(v_1, v_2)$, the reader is referred to Beirlant et al. (2004, Sect. 9.2).

For the likelihood inference, in principle two different models are available: The point-process method and the censored likelihood method. A major drawback of the point-process method is that $1 - F_j(d_j)$ must be small for all components, which means that both variables must be in the tail of the distribution. For additional drawbacks of this model, see Beirlant et al. (2004, Sect. 9.4.2). In contrast, the censored likelihood model can also capture the case when $1 - F_j(d_j)$ is small only for one component (here, when $1 - F_j(d_j)$ is small for only one day) or even no component. Using the previously defined bivariate threshold vector, the bivariate plane can be divided into four regions, which can be seen in Fig. 3.

The corresponding likelihood contributions can be written as:

$$l(d_1, d_2; \boldsymbol{\theta}_1, \boldsymbol{\theta}_2) \propto \begin{cases} F(u_1, u_2) & \text{if } d_1 \leq u_1, d_2 \leq u_2, \\ \frac{\partial F}{\partial d_1}(d_1, u_2) & \text{if } d_1 > u_1, d_2 \leq u_2, \\ \frac{\partial F}{\partial d_2}(u_1, d_2) & \text{if } d_1 \leq u_1, d_2 > u_2, \\ \frac{\partial^2 F}{\partial d_1 \partial d_2}(d_1, d_2) & \text{if } d_1 > u_1, d_2 > u_2. \end{cases} \quad (12)$$

The joint density can be modelled using the full tail dependence model of Eq. (9) as described in Beirlant et al. (2004)

$$l(d_1, d_2) = \begin{cases} \exp(-l^*(\phi_1, \phi_2)) & \text{if } d_1 \leq u_1, d_2 \leq u_2 \\ -\frac{\partial v_1}{\partial d_1} l_1^*(v_1, \phi_2) \exp(-l^*(v_1, \phi_2)) & \text{if } d_1 > u_1, d_2 \leq u_2, \\ -\frac{\partial v_2}{\partial d_2} l_2^*(\phi_1, v_2) \exp(-l^*(\phi_1, v_2)) & \text{if } d_1 \leq u_1, d_2 > u_2, \\ \exp(-l^*(v_1, v_2)) \frac{\partial v_1}{\partial d_1} \frac{\partial v_2}{\partial d_2} (l_1^*(v_1, v_2) l_2^*(v_1, v_2) - l_{12}^*(v_1, v_2)) & \text{if } d_1 > u_1, d_2 > u_2. \end{cases} \quad (13)$$

where the indices on l^* denoting partial derivatives. Thus, for every pair of consecutive time series points (d_i, d_{i+1}) , $l(d_1, d_2)$ must be evaluated (replacing (d_1, d_2) by (d_i, d_{i+1})). For the univariate likelihood $l(d_i; \theta_1)$, we can write

$$l(d_i; \theta_1) = \begin{cases} \frac{\phi_u}{\sigma_u} \left(1 + \xi \frac{d_i - u}{\sigma_u}\right)_+^{-1/\xi-1}, & \text{if } d_i > u, \\ 1 - \phi_u, & \text{if } d_i \leq u. \end{cases} \quad (14)$$

Finally, the parameters θ_1 and θ_2 must be fitted using the likelihood in Eq. (8). Due to the conditional stationarity assumption of the Markov model, the marginal distribution is the same for both variables and only needs to be fitted once.

3.3 Including non-stationarity

3.3.1 Can extremes be attributed, and is their frequency increasing over time? - Using a constant threshold

Since we are modelling exceedances in a non-stationary time series, we need to include slow changes over time into our likelihood formulation and, in particular, into the marginal parameters of the Markov process. In our first attribution approach, exceedances are modelled over a constant threshold u . The non-stationarity is modelled using slowly varying covariates, here given as low order Legendre polynomials as proposed in Min and Hense (2006). Legendre polynomials have several advantages. They are orthogonal, data independent, and smooth, so they are suitable to model slow non-linear trends.

We model the scale parameter $\sigma_{t_i} = \exp(\zeta_\sigma^T \mathbf{g}_t)$ and the shape parameter $\xi_{t_i} = \zeta_\xi^T \mathbf{g}_t$ as a linear combination of the Legendre polynomials $\mathbf{g}_t = (g_0(t), g_1(t), \dots, g_k(t))^T$ at time t , where k is the maximum order of polynomial degree included, and $\zeta_\sigma = (\zeta_{\sigma,0}, \dots, \zeta_{\sigma,k})^T$ and $\zeta_\xi = (\zeta_{\xi,0}, \dots, \zeta_{\xi,k})^T$ are the vectors of the regression coefficients.

Since the exceedance probability $\phi_{t_i}^u = \mathbb{P}(d_{t_i} > u)$, previously denoted with ϕ_u for the stationary case, also varies over time, we model the non-stationarity using a logistic regression again with Legendre polynomials as covariates. Logistic regression is a special case of a generalised linear model (Nelder and Wedderburn, 1972). We define the logistic regression using a logit link function such that

$$\text{logit}(\phi_{t_i}^u) = \log \left(\frac{\phi_{t_i}^u}{1 - \phi_{t_i}^u} \right) = \beta_u^T \mathbf{g}_t, \quad (15)$$

with \mathbf{g}_t the Legendre polynomials at time t and $\beta_u = (\beta_{u,0}, \dots, \beta_{u,k})^T$ the regression coefficients.

The dependence parameter α is assumed to also vary over time assuming that the dependence structure between two consecutive days can change slowly over time. Here, we allow a maximum degree of $k = 2$. Using a sigmoid link function to ensure α between 0 and 1, we can write

$$\alpha_{t_i} = \frac{1}{1 + \exp(-\boldsymbol{\varsigma}_\alpha^T \mathbf{g}_t)}. \quad (16)$$

For the parameter vector, we can now write $\boldsymbol{\theta} = (\boldsymbol{\beta}_u, \boldsymbol{\varsigma}_\sigma, \boldsymbol{\varsigma}_\xi, \boldsymbol{\varsigma}_\alpha)$.

3.3.2 Are the extremes becoming more extreme? - Using a variable threshold

Since large parts of the attribution statement are due to changes in the probability of exceeding the threshold u , we would like to exclude this effect. The attribution question that we ask in this case is as follows. Do extremes become more extreme? To model only distributional changes of extremes over a time-varying threshold u_t , we define u_t such that the probability $\mathbb{P}(d_t > u_t) = \tau$ is constant. We achieve a constant threshold exceedance by defining u_t as the conditional τ -quantile using quantile regression (Koenker and Machado, 1999; Koenker, 2005). This idea is based on Beirlant et al. (2004, Sect. 7.4.2), who suggest quantile regression to obtain a threshold value that depends on covariates. Moreover, as Chavez-Demoulin and Davison (2012) have pointed out, the use of a time-dependent threshold is to be preferred in order to achieve a more precise estimation of regression effects. Therefore, two models must be estimated: one for the quantile and one for the extremes.

Quantile regression assumes a linear model for the conditional quantile u_t using $u_t = \boldsymbol{\beta}_\tau^T \mathbf{g}_t$ with \mathbf{g}_t the Legendre polynomials at time t . The regression coefficients $\boldsymbol{\beta}_\tau$ are estimated using the check function

$$\rho_\tau(d_t - u_t) = \begin{cases} \tau(d_t - u_t) & \text{if } d_t \geq u_t \\ (\tau - 1)(d_t - u_t) & \text{if } d_t < u_t. \end{cases} \quad (17)$$

and by minimising the cost function

$$Q_\tau = \frac{1}{n} \sum_{i=1}^n \rho_\tau(d_{t_i} - u_{t_i}). \quad (18)$$

The scale parameter $\sigma_{t_i} = \exp(\boldsymbol{\varsigma}_\sigma^T \mathbf{g}_t)$ and the shape parameter $\xi_{t_i} = \boldsymbol{\varsigma}_\xi^T \mathbf{g}_t$ are again modelled as a linear combination of the Legendre polynomials, based on the exceedances over the time-varying threshold determined by quantile regression. Since $\phi_{t_i}^{u_i} = 1 - \tau$ is constant, the parameter vector is simplified to $\boldsymbol{\theta} = (\boldsymbol{\varsigma}_\sigma, \boldsymbol{\varsigma}_\xi, \boldsymbol{\varsigma}_\alpha)$.

3.4 Fitting procedure

The Markov process model is fitted according to Smith et al. (1997). We follow Beirlant et al. (2004) and first fit the marginal and dependence structure separately by introducing the covariates into the parameter estimation, as mentioned before. The optimal degree for the logistic regression (constant threshold) and the quantile regression (time-varying threshold) is then determined by the Bayesian information criterion (BIC). Then the GPD is fitted non-stationary in order to find the optimal degree of scale and shape parameter using the BIC. With the optimal degree of the Legendre polynomials for each parameter

determined by the BIC criterion, we fit the model jointly using the previously estimated parameters separately as starting values for the parameters, as suggested by Beirlant et al. (2004). Some advantages of the joint fit are mentioned by Beirlant et al. (2004), which are a better inference of the marginal parameters and a more reliable estimation of the dependence parameters.

4 Attribution statements for ERA5 using ensemble simulations

4.1 Model estimation with constant threshold

To determine the likelihood, we need to estimate the parameter vectors for our scenarios m_s , where $s = 1$ refers to HIST and $s = 0$ to HIST-NAT as described in Sect. 2. We assume that the ensemble simulations are independent realisations of the non-stationary temporal process under the respective scenario s . To estimate the parameters, we calculate the EPI for each realisation and both scenarios, then pool the realisations and estimate the parameter vectors $\beta_u^{(s)}, \varsigma_\sigma^{(s)}, \varsigma_\xi^{(s)}, \varsigma_\alpha^{(s)}$. The estimates are then used to derive the probability $\phi_{t_i}^{(s)}$ of exceeding the threshold u , the respective GPD parameters of the exceedances $\sigma_{t_i}^{(s)}$ and $\xi_{t_i}^{(s)}$, and the dependence parameter $\alpha_{t_i}^{(s)}$. The process of parameter estimation necessitates the implementation of a series of steps and the formulation of specific decisions:

1. First, the threshold u must be determined. It must be large enough to achieve asymptotic behaviour (Coles, 2001, Sect. 4.3.1), but small enough to allow sufficient data for reliable parameter estimation. In our application, we decided to use the 95% quantile of the respective ensemble simulations for the period 1940 to 2020 (HIST-NAT) and 1940 to 2025 (HIST & SPP2-4.5). The threshold $u^{(s)}$ is therefore scenario dependent. The advantage is that constant biases in the data are disregarded, and only the temporal evolution is investigated.
2. In a next step, we estimate the time-varying exceedance probability $\phi_{t_i}^{(s)}$ over the constant threshold $u^{(s)}$ using logistic regression (see Sect. 3.3.1) for both scenarios, respectively. To determine the optimal maximum degree of the Legendre polynomials, we used the BIC. The fitting is performed with the use of the statistical software package `statsmodels` (Seabold and Perktold, 2010).
3. The non-stationary GPD is estimated with `statsmodels` using maximum likelihood estimation. Again, the BIC is used to assess the optimal maximum degree of Legendre polynomials. Goodness-of-fit is assessed using quantile-quantile and probability-probability plots as described in Sect. 6.2.3 in Coles (2001). All combinations of scale and shape parameters up to degree five are allowed, in which the degree of the shape parameter is not allowed to be larger than the degree of the scale parameter ($\text{deg}(\sigma) \geq \text{deg}(\xi)$). Here, we use all threshold exceedances and do not apply a declustering scheme.
4. Next, the distribution of l^* must be specified, in this example the Logistic model. For the fitting, for each scenario the univariate estimates and $\phi_{t_i}^{(s)}$ and the optimal degree of $\sigma_{t_i}^{(s)}$ and $\xi_{t_i}^{(s)}$ are plugged into the censored likelihood approach. Then the optimal degree of the covariates for the dependence parameter is determined. Finally, using the estimated parameters as starting values, the model is fitted jointly and the resulting parameters are returned by the fit.

4.2 Likelihood of ERA5 with constant threshold

With the estimates $u^{(s)}$, $\phi_{t_i}^{(s)}$, and the parameters $\sigma_{t_i}^{(s)}$, $\xi_{t_i}^{(s)}$, and $\alpha_{t_i}^{(s)}$ given for each scenario s , we can derive the likelihood ratio of the reanalysis data \mathbf{d} given different scenarios from Eq. (5).

The likelihood ratio of \mathbf{d}_{ERA5} between the scenarios s_1 and s_0 is given as

$$LR = \frac{l(\mathbf{d}_{ERA5}; u_{ERA5}, \alpha_{t_i}^{(1)}, \phi_{t_i}^{(1)}, \sigma_{t_i}^{(1)}, \xi_{t_i}^{(1)})}{l(\mathbf{d}_{ERA5}; u_{ERA5}, \alpha_{t_i}^{(0)}, \phi_{t_i}^{(0)}, \sigma_{t_i}^{(0)}, \xi_{t_i}^{(0)})}, \quad (19)$$

with \mathbf{d}_{ERA5} containing the EPI of the ERA5 reanalysis. This LR leads to an attribution statement for a time period or the entire observed time series until a year to be chosen.

4.3 Model estimation with variable threshold

The attribution statement with a variable threshold u_t is different, since here we only look at the variable distribution above u_t . The variable threshold u_t is assumed to contain a large part of the anthropogenic climate change signal, which is thereby removed. According to Sect. 4.1, the likelihood of \mathbf{d} in scenario s is determined by the respective parameter vectors $\beta_{\tau}^{(s)}, \varsigma_{\sigma}^{(s)}, \varsigma_{\xi}^{(s)}, \varsigma_{\alpha}^{(s)}$. They are needed to derive the time-varying threshold u_t with the regression coefficients $\beta_{\tau}^{(s)}$, the marginal parameters $\sigma_{t_i}^{(s)}$ and $\xi_{t_i}^{(s)}$, and the dependence parameter $\alpha_{t_i}^{(s)}$ for each scenario s . Again, we pool the ensemble and describe the necessary steps and decisions for the model estimation.

1. The first step is to perform the quantile regression of the ensemble simulations for a sufficiently high quantile, in our case the 95% quantile, as selected in Sect. 4.1, leading to the time-varying thresholds $u_t^{(s)}$. Again, we make use of the BIC to derive the optimal maximum degree of the Legendre polynomials. The fitting is performed once again with the usage of the statistical software package `statsmodels`.
2. In principle, the steps are similar to those described in 4.1, but now use time-varying thresholds to account for the effect of the mean increase in the time series. For fitting the non-stationary GPD, once again the package `statsmodels` can be used, and the model evaluation is the same as mentioned in 4.1.
3. Again, the distribution of l^* must be specified, in this example the logistic model. For the fitting, for each scenario the univariate estimates $u_t^{(s)}$, and the optimal degree of $\sigma_{t_i}^{(s)}$ and $\xi_{t_i}^{(s)}$ are plugged into the censored likelihood approach in order to determine the optimal degree of the covariates for the dependence parameter. Finally, the model is fitted jointly with the parameters estimated separately as starting values.

4.4 Likelihood of ERA5 with variable threshold

Using the thresholds $u_t^{(s)}$ and the parameters $\sigma_{t_i}^{(s)}$, $\xi_{t_i}^{(s)}$ and $\alpha_{t_i}^{(s)}$ given for each scenario s , we can derive the likelihood ratio from Eq. (5). We can then write the likelihood ratio of \mathbf{d}_{ERA5} between the scenarios s_1 and s_0 :

$$LR = \frac{l(\mathbf{d}_{ERA5}; u_{t,ERA5}, \alpha_{t_i}^{(1)}, \sigma_{t_i}^{(1)}, \xi_{t_i}^{(1)})}{l(\mathbf{d}_{ERA5}; u_{t,ERA5}, \alpha_{t_i}^{(0)}, \sigma_{t_i}^{(0)}, \xi_{t_i}^{(0)})}. \quad (20)$$

with $u_{t,ERA5}$ as the time-varying threshold based on the 95% quantile regression of the ERA5 EPI time series over the period 1940 to 2025 (JJA).

4.5 Uncertainty assessment

According to Paciorek et al. (2018), uncertainties arise from different sources. Uncertainty with respect to internal climate variability is generally assessed using large climate model ensembles, whereas ensembles with different climate models as used in this study further assess model uncertainty. Additional uncertainty arises from the observations of the climate system, which, however, is generally small compared to other sources of uncertainty.

To account for sampling uncertainty, two approaches are often used. The delta-method and bootstrapping (Jeon et al., 2016). In this study, we use the bootstrap method. For the bootstrap method, we proceed as follows for each scenario (repeating this for both scenarios of each climate model):

1. Split the data set into yearly parts.
2. For each year, sample the indices with replacement from $\{0, 1, \dots, N_m\}$ with N_m the number of indices sampled, which is equal to the number of ensemble members.
3. For each year, the ensemble members corresponding to the selected indices are used.
4. All years are combined.

Using this bootstrap method, the attribution is then repeated N_B times for each of the climate models.

4.6 Combining different likelihood ratios

Due to the usage of different climate models, we may receive a set of different likelihood ratios for an event or a time series. One may ask which likelihood ratio should be favoured or how a combined likelihood ratio can be calculated, since when communicating attribution results, the interest often lies in a specific value rather than a range of possible values. We follow an approach presented by Otto et al. (2024) that aims to combine different pieces of evidences (i.e., logarithmic probability ratios in their study) using an approach also used in meta-analyses and known as the random-effects model. This model is based on a paper published by Paule and Mandel (1982).

The main idea is to decompose the total variability into a contribution from natural variability σ_{nat} and a model uncertainty σ_{mod} , which results in $\sigma_{tot}^2 = \sigma_{nat}^2 + \sigma_{mod}^2$. For each climate model, we have a best estimator of the likelihood ratio, denoted by $\hat{\mu}_i$ and an estimator for the variance $\hat{\sigma}_i$ based on the bootstrap approach as discussed in Sect. 4.5. The focus now lies on estimating the weights w_i for each climate model i , which represent the belief or confidence in the specific model given by

$$w_i(\sigma_{mod}) = \frac{1}{\hat{\sigma}_i^2 + \sigma_{mod}^2} \quad (21)$$

The best estimate of the likelihood ratio of the n climate models is then given by a weighted average

$$\hat{\mu}(\sigma_{mod}) = \frac{\sum_{i=1}^n w_i(\sigma_{mod}) \hat{\mu}_i}{\sum_{i=1}^n w_i(\sigma_{mod})}, \quad (22)$$

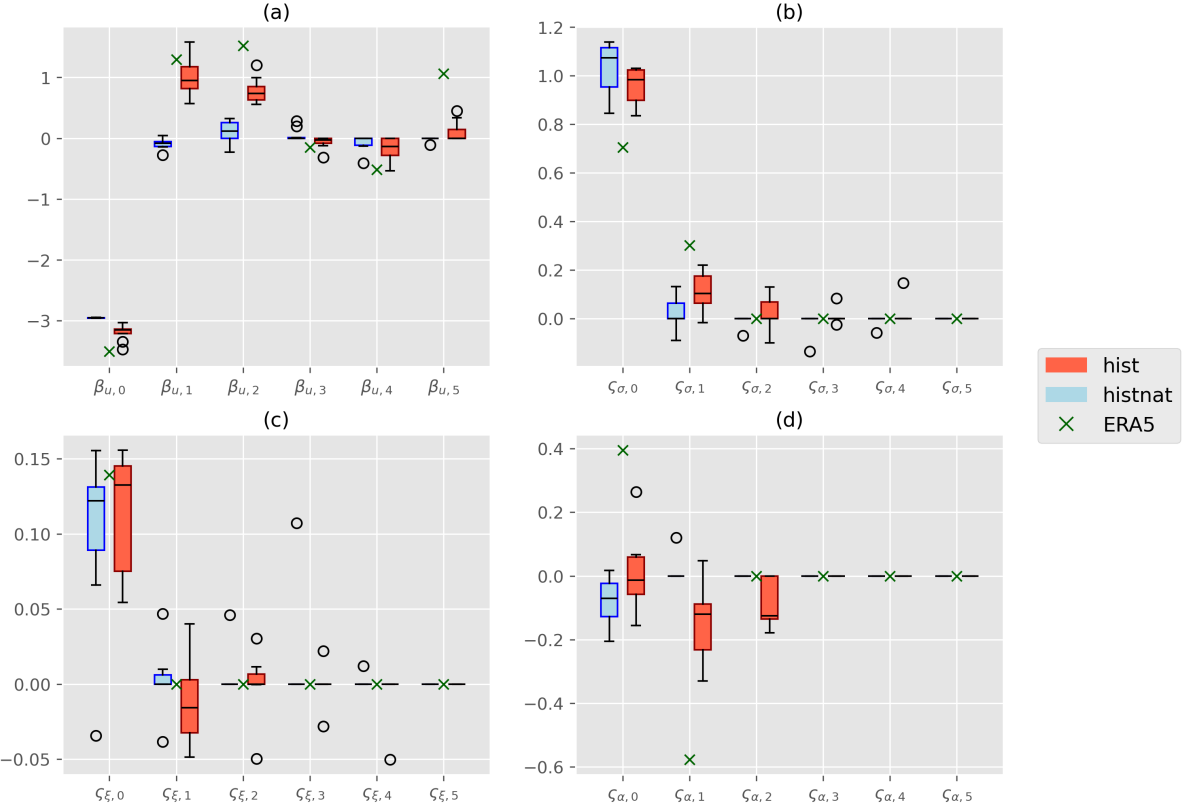


Figure 4. Estimated coefficients for the model with constant threshold (Sect. 4.1) in the southern European region. The coefficients (x-axis) are shown for (a) the threshold exceedance ϕ , (b) the scale σ , (c) the shape ξ , and (d) the dependence α . The estimates for the different climate models are represented as box-whiskers, those for ERA5 as green crosses. The whiskers and fliers cover the whole range of data.

and only a function of the model uncertainty or the representation error term σ_{mod} . For the combined uncertainty, we can write

$$\sigma_{tot}^2 = \frac{1}{\sum_{i=1}^n w_i} \sum_{i=1}^n w_i (\hat{\sigma}_i^2 + \sigma_{mod}^2). \quad (23)$$

5 Results

5.1 Model parameter estimation

According to Sect. 4, both models with constant and time-varying threshold are fitted to the data. For each climate model and scenario, we receive a set of parameter coefficients. Figure 4 shows the coefficient estimates of the model with a constant threshold (Sect. 4.1) for the EPI of the southern European region. The same model was also fitted to the EPI in ERA5 for comparison. The first coefficient in each panel always represents the intercept, the second is a linear trend over time, and the

third is a quadratic trend. For the HIST-NAT scenario simulations, we do not expect tendencies, and indeed the intermodel variability of the trend parameters generally includes the zero line.

For the HIST scenario simulations, the exceedance probability shows significant positive trends, particularly in the linear and quadratic Legendre polynomials. For some CMIP6 models the higher order polynomials contribute to the BIC, but the signals are not consistent between the models. The parameter estimates for the threshold exceedance parameters in ERA5 are close to the range spanned by the estimates of the CMIP6 models. The uncertainty in the ERA5 parameter estimation is significantly larger than in the CMIP6 models, as the latter are estimated using a simulation ensemble and not, as in ERA5, a single realisation. Consequently, the ERA5 estimators may lie outside the uncertainty range given by the models.

The scale parameter estimates in the HIST scenario shows a consistent linear increase, with a less consistent quadratic component. Again, ERA5 shows a similar behaviour in the non-stationarity of the scale parameter. The positive tendency in the scale parameter, however, is contour-acted by a negative linear trend in the shape parameter. This negative trend in the scale parameter is visible in most models, but not in ERA5. The overall positive shape parameter is expected in all scenarios, all simulations and in ERA5, since the input data are the EPI, and the EPI in turn relies on standard Fréchet transformed T2max values. For the dependence parameter, the linear and quadratic coefficients are relevant, while in ERA5 only the linear term is non-zero. Similar tendencies in the parameters are observed for the northern and central European region as shown in the Appendix (Sect. A3) in Figs. A6 and A7, with a similarly good agreement between CMIP6 simulations and ERA5.

The resulting temporal evolution of the parameters is shown in Fig. 5. The increasing threshold exceedance probability in the HIST scenario is clearly visible, with a strong increase starting in the 80s as a consequence of the 2nd order Legendre polynomial. A similar trend, with an even stronger increase during the last decade, is visible for the ERA5 threshold exceedance probability. The scale parameter increases in the HIST scenario. Although this trend is stronger and starts from a lower level, it is consistent with the trend in ERA5. The trends in the shape parameter show large uncertainties between the different CMIP6 models. The ERA5 shape parameter is at the upper uncertainty level of the models and could counteract the effect of the comparatively low scale parameter.

The increasing dependence (i.e., decreasing α) is visible for the HIST scenario and ERA5. The dependence in ERA5 is weaker at the beginning, and the trend toward increasing dependence is significantly stronger compared to the HIST scenario. The increasing dependence is a direct consequence of the rising probability of exceedance, which leads to a higher frequency of consecutive heatwaves.

Figure 6 shows the coefficient estimates of the model with time-varying threshold (Sect. 4.3) for the EPI of the southern European region. In the model with a time-varying threshold, there are no coefficients for the threshold exceedance probability, since this is constant by definition. Instead, we display the quantile regression parameters, which contain a large part of the non-stationarity, but which are not part of the likelihood model.

For the HIST-NAT scenario, the model variability of the trend parameters includes the zero line, similar to the model with a constant threshold. For the HIST scenario, the linear and quadratic coefficients of the quantile regression are significantly different from zero and thus show a positive trend. ERA5 exhibits similar behaviour to that of the HIST scenario.

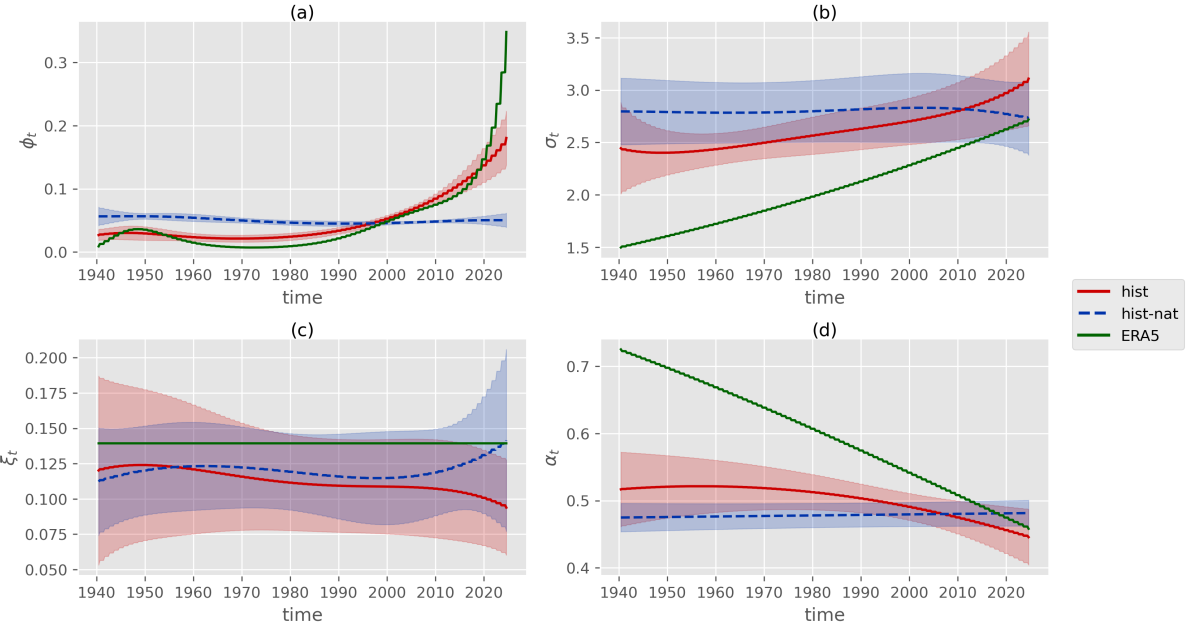


Figure 5. Temporal evolution of (a) threshold exceedance probability, (b) scale, (c) shape, and (d) dependence parameters for the model with constant threshold in the southern European region. Mean (solid line) and standard deviation (shading) for the different climate models is plotted based on the estimates in Fig. 4.

For the scale and shape parameters, the linear and quadratic coefficients become relevant. While the coefficients indicate a positive trend in the scale parameter in the HIST scenario, the trend for the shape parameter is negative. Higher-order coefficients are only relevant for a subset of the climate models in the HIST scenario. In contrast, for ERA5 only the first order Legendre polynomial becomes relevant for the scale parameter, while the shape parameter is stationary. In terms of dependence, the linear coefficient is relevant in the HIST simulations and in ERA5, suggesting a decrease in dependency.

The resulting temporal evolution of the parameter estimates (Fig. 7) of the HIST-NAT scenario does not show significant trends. An increase in the threshold is visible for the HIST scenario and in ERA5, which is a consequence of the general warming trend. In this HIST scenario, the scale parameter also increases with time. In contrast, the shape parameter initially increases until about 1970, then decreases and becomes negative for most of the climate models after 2010. This behaviour is not reflected by ERA5. A weak decrease in dependence can be observed in the second half of the time series in the HIST scenario.

The negative shape parameter ($\xi < 0$) in the HIST scenario means that the exceedances are bounded above, with an upper limit of $u - \sigma/\xi$ (Coles, 2001, Sect. 4.2.1). We therefore observe that the distribution of exceedances of the time-dependent 95% quantile becomes light-tailed over time. This effect is partially offset by the increases in the scale parameter. It can thus be concluded that although the variance of the exceedances increases, the probability of large outliers decreases. However, the tendency toward a negative shape parameter may also indicate that the transformation to standard Fréchet, as required to

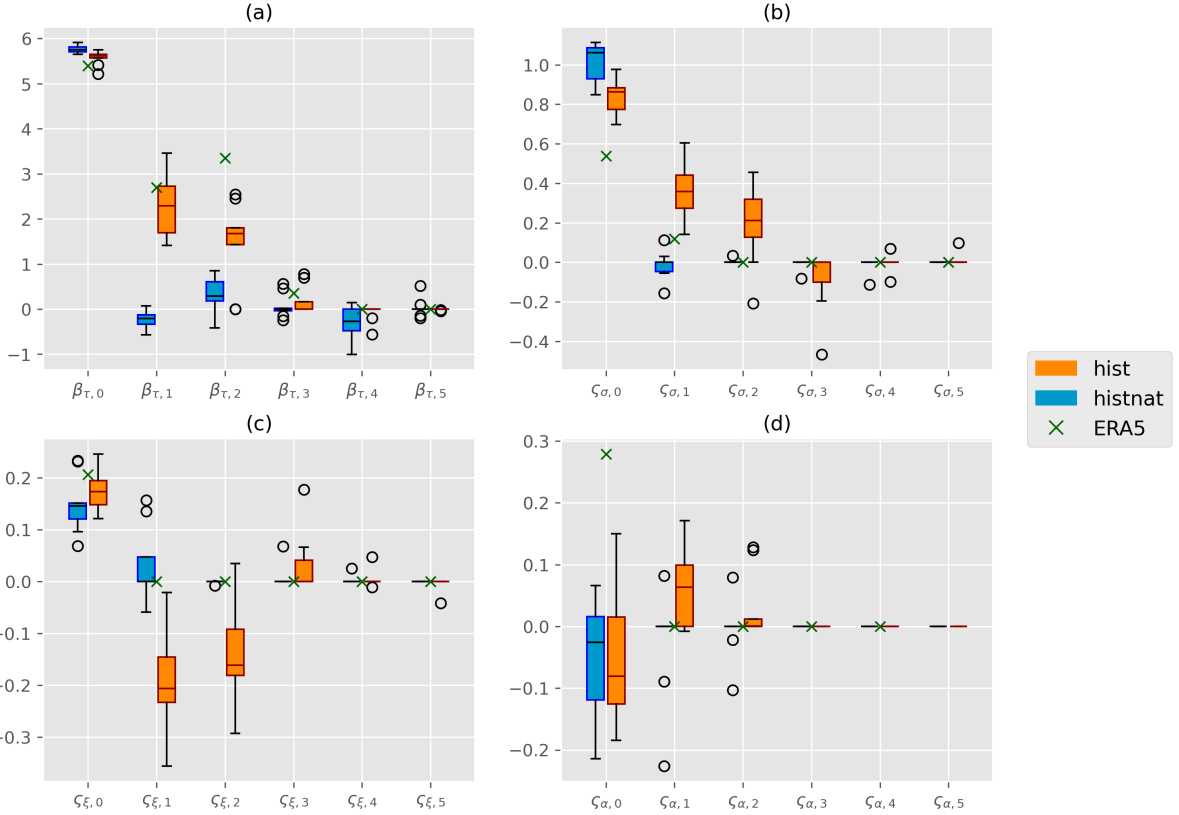


Figure 6. Same as Fig. 4 but for the model with time-varying threshold (Sect. 4.3) in the southern European region, except that (a) shows the quantile regression parameters of the time-varying threshold.

determine the EPI, no longer works, and that the strong non-stationarity must therefore be taken into account when defining the spatial patterns.

What we can show is that the sign change of the shape parameter in this model shows a significant improvement in BIC compared to a model that either keeps the shape parameter constant or restricts it to the positive value range. Very similar tendencies, particularly the negative trend in the shape parameter is also observed for the other regions, as shown and described in the Appendix in Sect. A3 in Figs. A8 and A9.

5.2 Attribution results

Given the parameters estimates of the non-stationary Markov models, we can calculate the likelihood ratios in Eq. (19) and (20) according to Sect. 4.6. Figure 8 shows the logarithmic likelihood ratios for both the models with constant and variable threshold, and the respective standard deviations for summers in the northern European region since 2000. The first event that provided substantial evidence for the HIST scenario was in 2010, and two events in 2018 and 2022 even show strong evidence

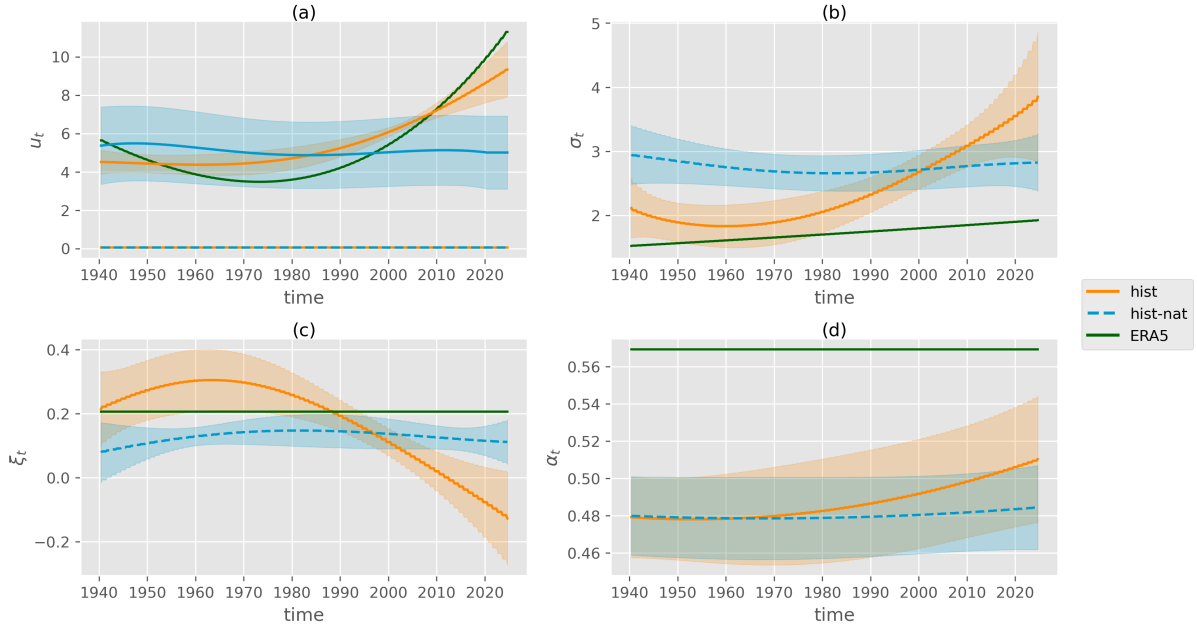


Figure 7. Same as Fig. 5 but for the model with time-varying threshold in the southern European region.

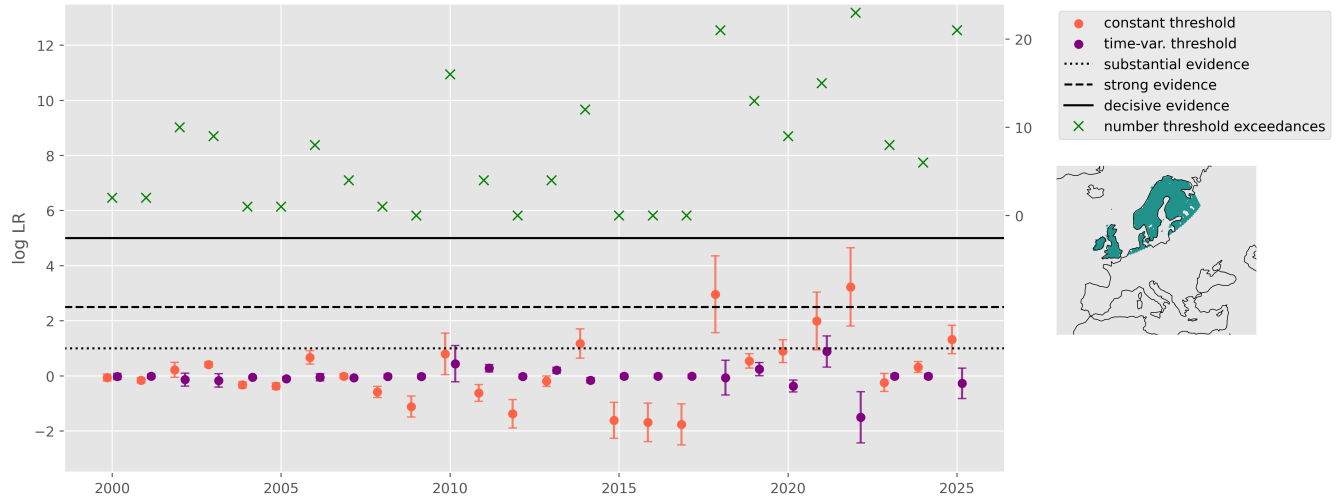


Figure 8. Logarithmic likelihood ratio including \pm standard deviation (y-axis left) for the northern European region, estimated according to Sect. 4.6. Green crosses indicate the number of threshold exceedances of the ERA5 EPI over the 95%-quantile in the respective summer (y-axis right).

for a single northern European summer time series. All events are documented as extreme heat events. The likelihood ratio of the summer 2025 is not in the top three highest likelihood ratios. This might be surprising, since the July 2025 heatwave was

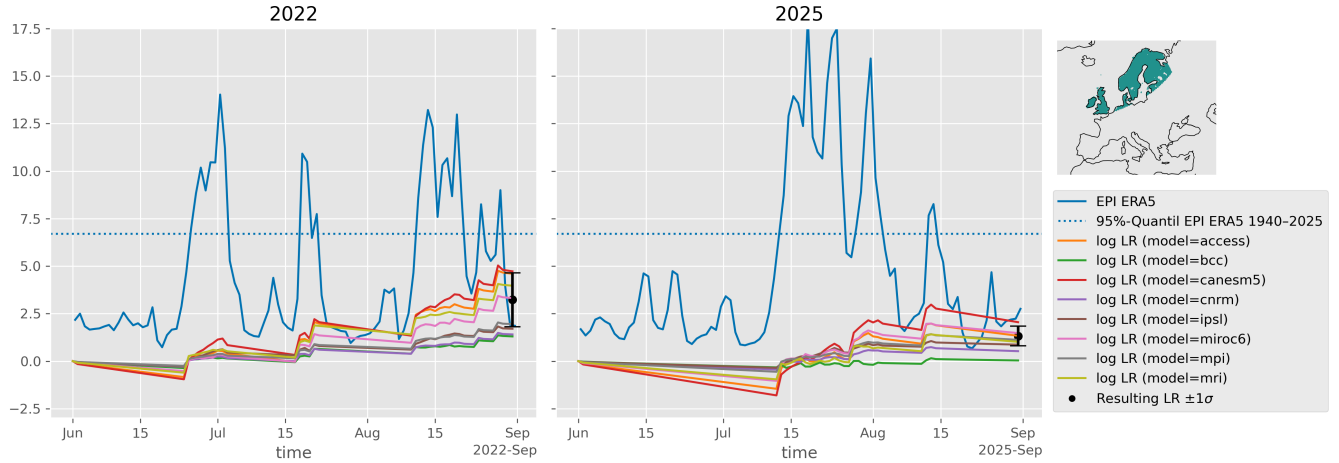


Figure 9. EPI of ERA5 and the logarithmic likelihood ratio for the summers 2022 and 2025 in the northern European region and the constant threshold model. The estimate shown in Fig. 8 is marked in black.

exceptional, as documented by Barnes et al. (2025). Our attribution refers to the entire summer period with a relatively cold June, which reduces the corresponding likelihood ratio (Fig. 9), whereas the attribution in Barnes et al. (2025) only considers the hot phase in July. Compared to summer 2022, which has a similar number of threshold exceedances, the resulting likelihood ratio of the summer 2025 is higher due to the different types of heatwave. In 2022, there were three heat events, whereas in 2025 there was only one (see Fig. 9), which affects the attribution result, since the Markov transitions are different. In general, we can conclude, that the attribution result is affected by not only the number of threshold exceedances (as shown in Fig. 8) but also the type (short- or long-term events) of the event, the number of events and the strength of the EPI.

For the model with a time-varying threshold, in the northern European region, most summers have a logarithmic likelihood ratio of approximately zero (i.e., a likelihood ratio of one). This means that no other effect apart from a general increase in the threshold value can be detected in the northern European region. The significant difference in the likelihood ratios between 2021 and 2022 is due to the much higher EPI values observed during the heat events in 2021 compared to 2022.

For the central European region, Fig. 10 shows more years with a logarithmic likelihood ratio indicating strong evidence than in the northern European region. The summer 2010 with the heatwave over eastern Europe and Russia is already outstanding in terms of threshold exceedances. The highest likelihood ratios are observed for the summers in 2010, 2012, 2015, 2019, 2022, and 2025. All of these years fall into the *strong* category and are considered to be summers with heat waves. The compound heat and drought event in 2018 (Xoplaki et al., 2025) has a much smaller likelihood ratio, with also a lower number of threshold exceedances. In terms of maximum temperature, the summer 2018 in central Europe was not as extreme as the other years. The severe impacts in this summer are mainly due to the combination of high temperatures and drought. The variable threshold model again provides no evidence beyond a trend in the threshold, except maybe for the summer in 2019.

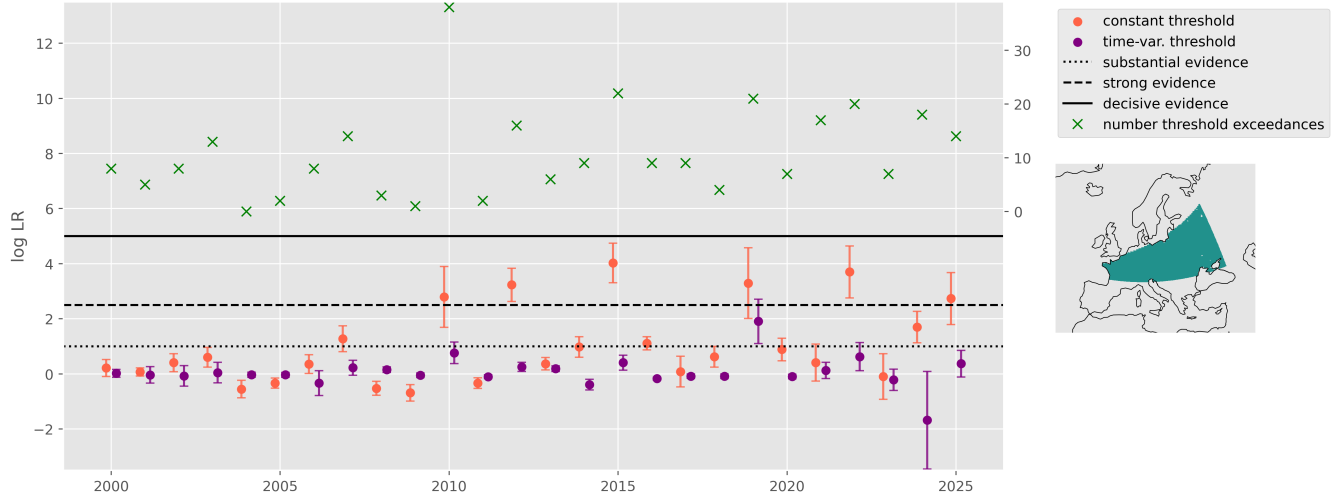


Figure 10. Same as Fig. 8 but for the central European region.

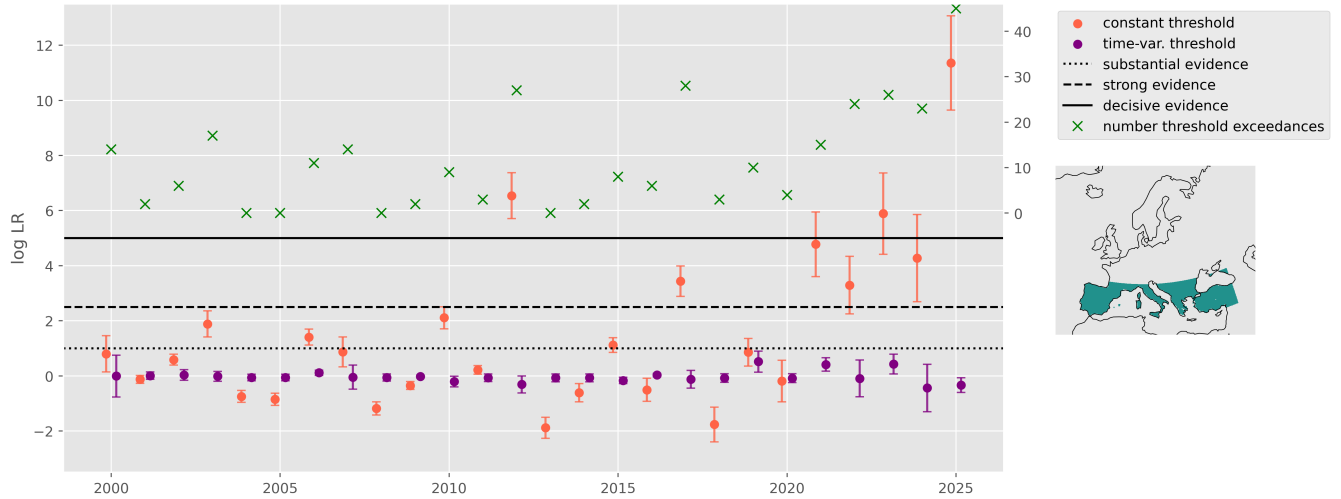


Figure 11. Same as Fig. 8 but for the southern European region.

In the southern European region (Fig. 11), the year 2025 was outstanding compared to the other years. On almost half of the summer days, the EPI for the southern European region exceeded the 95th percentile, while the summer was similar to the summer of 2024 in terms of average maximum summer temperatures. High likelihood ratios can be observed primarily since 2021, with the summers of 2012, 2023, and 2025 are into the *decisive* category. The southern European region clearly shows the strongest evidence of climate change among the three regions.

When the effect of the variable threshold is eliminated, the logarithmic likelihood ratio fluctuates around one in all regions. However, uncertainty appears to increase with higher threshold values, which can cause both downward and upward excursions

over a period of several years. The negative shape parameter of the variable threshold model observed in the anthropogenic-driven simulations after 2010 is not observed in ERA5 and could therefore be an artifact of the numerical models. Alternatively, this could indicate possible changes in processes that are not yet apparent in the ERA5 data but occur in climate simulations under the driving scenario. It is therefore also possible that the modelled trends in the CMIP6 simulations are not yet observable in ERA5.

Years with a high probability ratio in the time-dependent threshold model are usually years with many event/non-event transitions, where the EPI exceeds the threshold on only one of two consecutive days. Such events become more likely in the HIST scenario due to the change in the shape and dependency parameters. This applies to all three regions, as the parameters and their trends are similar for the different regions.

Finally, we are interested in the question of when in the past we would have had sufficient evidence for climate change using the means available to us today. To answer this question, we use equation (7) with uniform prior probabilities and obtain

$$\frac{\mathbb{P}(m_1 | \mathbf{d}^{(n)}, \dots, \mathbf{d}^{(1)})}{\mathbb{P}(m_0 | \mathbf{d}^{(n)}, \dots, \mathbf{d}^{(1)})} = \prod_{i=1}^n \text{LR}(\mathbf{d}^{(i)}). \quad (24)$$

Using this equation, we can calculate the likelihood ratio of the different scenarios when considering all summers up to a given year n , starting with 1940 and ending with 2025. If the likelihood ratio in Eq. (24) exceeds the value of 150 (see Table 2), we conclude that there is decisive evidence against the HIST-NAT scenario after the summer of the year n .

For the model with constant threshold, the level of decisive evidence is reached in 1961 in the central European region and in 1964 in the southern European region. For the northern European region, the probability ratio has repeatedly fallen below this value since 1940. However, since 2021, it has remained consistently above 150. For the central and southern European regions, the likelihood ratio since 1940 has an increasing trend throughout the time period. For example, after the summer of 2025, we found for the southern European region a value of

$$\frac{\mathbb{P}(m_1 | \mathbf{d}^{(2025)}, \dots, \mathbf{d}^{(1940)})}{\mathbb{P}(m_0 | \mathbf{d}^{(2025)}, \dots, \mathbf{d}^{(1940)})} \approx 2.25 \cdot 10^{26}. \quad (25)$$

In other words, the probability of the scenario with anthropogenic emissions given the summers from 1940 to 2025 is 10^{26} times higher than the probability of the scenario without anthropogenic emissions given the summers from 1940 to 2025. For the model with a time-varying threshold, we can still attribute the entire period from 1940 onwards to the HIST scenario. As can be seen in Fig. 12, after an overall increase in the likelihood ratio from 1940 to 1980, it remains almost constant thereafter. This implies that summers after 1980 do not provide additional evidence for the HIST scenario in the model with a time-varying threshold, and all support for the HIST scenario is due to the period where we do not expect an anthropogenic climate change signal.

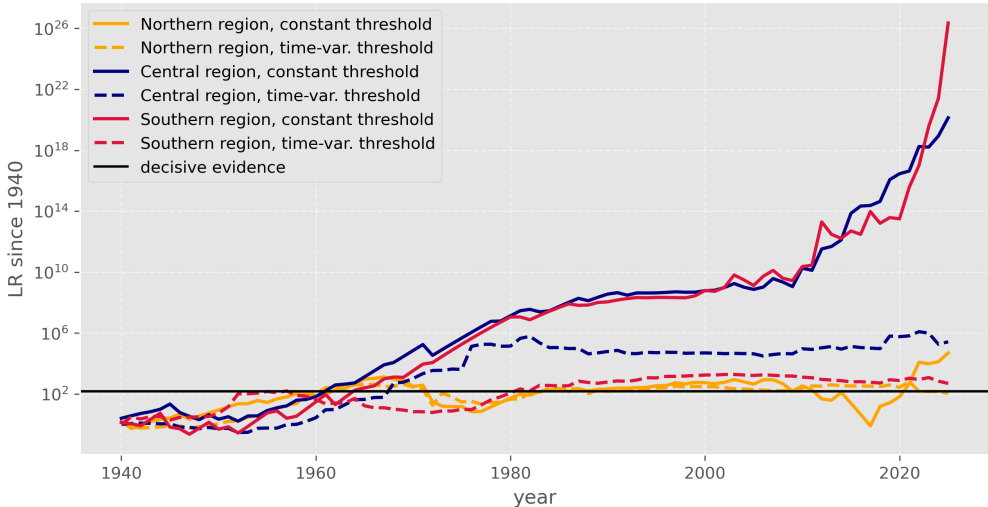


Figure 12. Accumulative likelihood ratio for all summers since 1940 up to a given year n (x-axis). This Figure is based on Eq. (7), when assuming that the prior probability of both scenarios are equal.

6 Discussion and conclusion

The Markov process model, which is based on bivariate extreme value theory, has been shown to be suitable for modelling the temporal dependence of the EPI, and thus deriving likelihood of the observed EPI in ERA5 given different scenarios. Due to the Markov assumption, time periods ranging from two days to several years can be considered for attribution.

The non-stationarity of the Markov process allows us to examine the temporal changes in the time series due to climate change. To our knowledge, the adaptation of the censored threshold model to the non-stationary case is new and has not been used before. With a second model featuring a constant exceedance probability and a corresponding time-dependent threshold value, we can also answer the question of whether climate signals exist in the behaviour of extremes that go beyond a mean increase in the threshold value.

Our approach enables us to statistically model the temporal development of extreme events and thus also to conduct a corresponding attribution study. For heatwaves in Europe, there is a clear answer to the question whether their temporal evolution can be attributed to anthropogenic emissions: The entire summer time series of the EPI from ERA5 can be assigned to the HIST scenario for each region with decisive evidence. Since 2000 in particular, heatwave events have increased in frequency, and the number of summers that can be attributed to the HIST scenario with strong or decisive evidence has risen. In the central and southern European region, decisive evidence in favour of the scenario with anthropogenic emissions has been available since the 1970s, when considering all summers since 1940.

There is no clear answer to the second question, whether extremes are becoming more extreme. In the first half of the time series, an increasing shape parameter in the HIST scenario supports this hypothesis. However, the estimated non-stationarities over the last three decades significantly differ between the HIST scenario simulations and ERA5 in the variable threshold

model. The trend towards a negative shape parameter in the HIST scenario suggests an upper endpoint for extremes, albeit counteracted by an increased scale parameter. In addition, the shape parameter is only slightly negative, so the upper bound only applies to very extreme observations. Both is not reproduced in ERA5. Particular summers with many event/no event pairs are attributed to the HIST scenario, since the respective CMIP6 model shape parameter estimates make these events more likely. All support for the HIST scenario is due to the period where we do not expect an anthropogenic climate change signal.

In the Appendix, we further examine the influence of a seasonal cycle that may still be present in the data on attribution (Appendix A1) and an extension of the model to a Markov process in Appendix A2. Since both extensions have only a minor influence on the attribution statement, the results are not included in the main body of the article.

To summarise, the main contribution of this paper lies in the extension of the censored likelihood model for extremes to non-stationary time series, and its application to the attribution of the evolution of heatwaves over different regions in Europe. The significant non-stationarities in the temperature data is an issue for any extreme value model. A constant threshold model needs to be handled with care in the presence of strong temporal trends. This indicates the strong effect of the non-stationarity in the constant threshold model on the dependencies.

Our second approach uses a time-varying threshold value to eliminate its effect and evaluate changes beyond it. However, the peak-over-non-stationary threshold model by Friederichs (2010) can also be adapted so that it can be used for extreme dependencies in time series, and thus also, for example, for attribution in Eq. (20). The main difference to Friederichs (2010) in this article is that the time-varying threshold model uses a threshold estimated on ERA5 data to remove the ERA5 warming trends. The significantly stronger non-stationarities in future climate projections require sophisticated statistical extreme value models that adequately account for non-stationarities. This work is therefore an important step toward the statistical evaluation of non-stationary time series for extremes in the past and future.

Appendix A

A1 Including seasonal cycle in parameter estimation

Although the seasonal cycle is removed when calculating the TPDM, a residual seasonal cycle remains in the EPIs, which can be shown. One way to account for this is to model this residual seasonal cycle when fitting the parameters. Here, we assume that the seasonal cycle can be described using sine- and cosine functions. For parameter estimation in the model with a constant threshold (Sect. 4.1), we can write:

$$\sigma_{t_i} = \exp(\boldsymbol{\varsigma}_\sigma^\top \mathbf{g}_t + \delta_1 h_1(\text{doy}) + \delta_2 h_2(\text{doy})) \quad (\text{A1})$$

$$\xi_{t_i} = \boldsymbol{\varsigma}_\xi^\top \mathbf{g}_t + \delta_3 h_1(\text{doy}) + \delta_4 h_2(\text{doy}) \quad (\text{A2})$$

$$\text{logit}(\phi_{t_i}^u) = \beta_u^T \mathbf{g}_t + \delta_5 h_1(\text{doy}) + \delta_6 h_2(\text{doy}) \quad (\text{A3})$$

$$\alpha_{t_i} = [1 + \exp(-\varsigma_\alpha^T \mathbf{g}_t + \delta_7 h_1(\text{doy}) + \delta_8 h_2(\text{doy}))]^{-1} \quad (\text{A4})$$

with $h_1(\text{doy}) = \sin(2\pi \text{doy } T^{-1})$, $h_2(\text{doy}) = \cos(2\pi \text{doy } T^{-1})$, and $T = 365.25$. doy is the day of the year and δ_i the model coefficients to be additionally estimated. For the model with a time-varying threshold, the procedure is similar. However, for the sake of simplicity, we have chosen not to introduce a seasonal cycle into the quantile regression. The workflow of fitting the models is then the same as described in Sect. 4. Based on the maximum temperature example in the southern European region, the modelled seasonal cycle is plotted for models with constant and time-varying thresholds in Fig. A1 and A2.

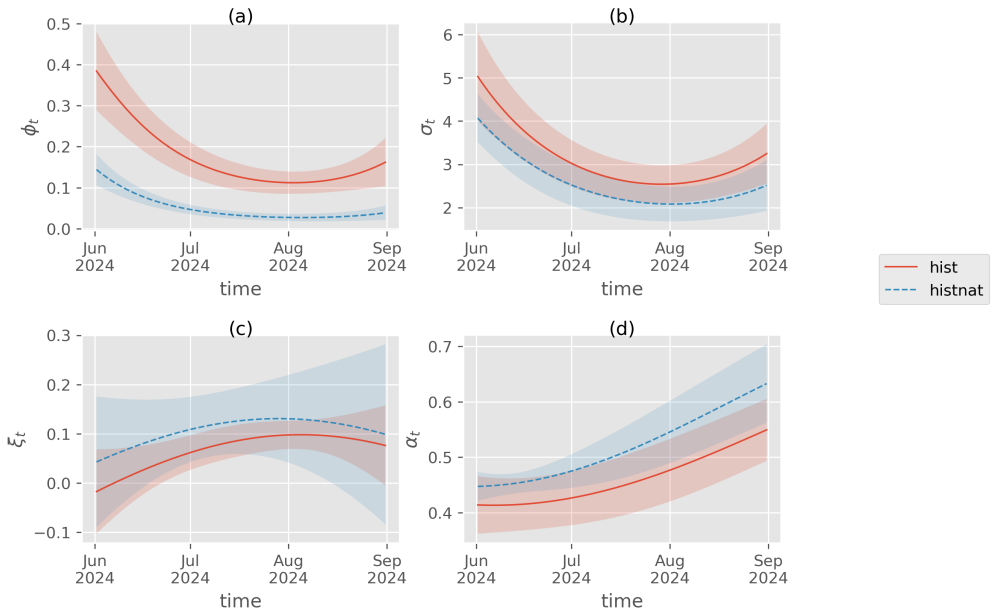


Figure A1. The seasonal cycle of (a) threshold exceedance probability, (b) scale, (c) shape, and (d) dependence parameters for the southern European region is shown for the year 2024, with mean and standard deviation calculated based on the different climate models.

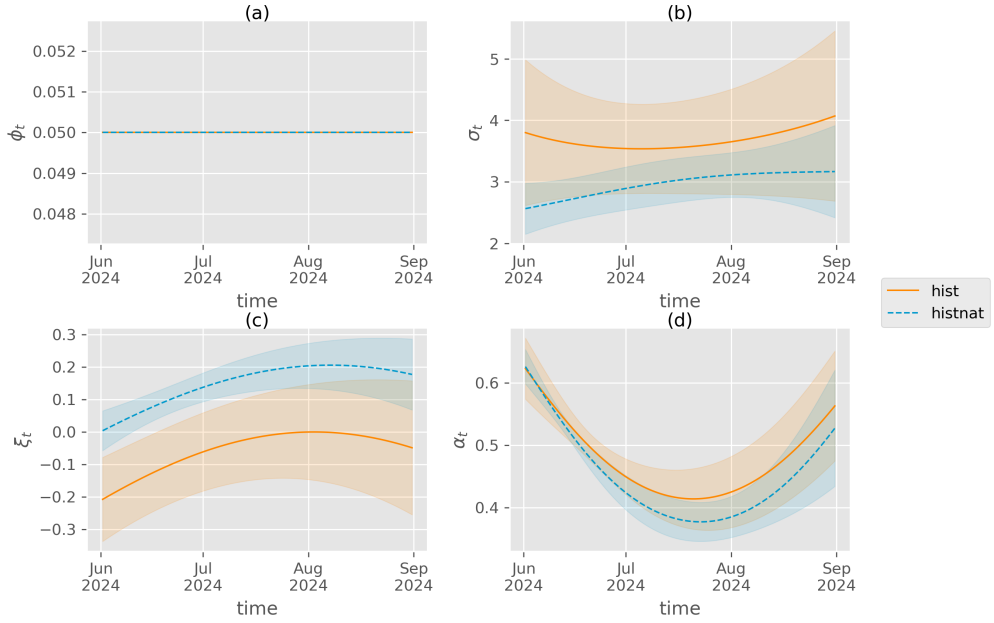


Figure A2. Same as Fig. A1 but for the model with time-varying threshold.

The seasonal cycle is similar for both models and scenarios. This suggests that the seasonal cycle may not shift significantly in response to climate change. However, the seasonal cycle shown here should be interpreted with caution, as it is a residual cycle remaining after the seasonal cycle has been removed from the data to calculate the TPDM. To evaluate the effect of modelling the seasonal cycle on the estimation of the likelihood ratio, we calculate the likelihood ratio for each summer both with and without the seasonal cycle (as before).

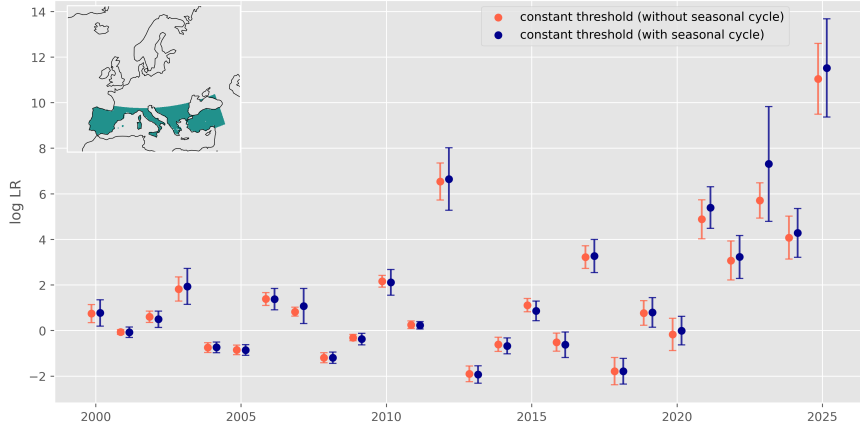


Figure A3. Logarithmic likelihood ratio including \pm standard deviation for the northern European region, estimated according to Sect. 4.6, for the model with a constant threshold with and without modelling the seasonal cycle. For simplicity, no random effect model is used; instead, only the mean and standard deviation for the various models are displayed.

The resulting likelihood ratios (Fig. A3) have been similar for many years, with slightly higher likelihood ratios (and greater uncertainty) observed for the last five years when modelling the seasonal cycle. However, the effect of modelling the seasonal cycle is limited.

A2 Second order Markov process

Aside from modelling the seasonal cycle, the first-order assumption of the Markov process may be questionable. To investigate the effect of this choice, we expand the analysis to include a second-order Markov process to capture dependencies on a longer timescale. To this end, we can rewrite Eq. (8) to

$$l(\mathbf{d}; \boldsymbol{\theta}) = l(d_1, d_2; \boldsymbol{\theta}_1, \boldsymbol{\theta}_2) \prod_{i=3}^n l(d_i | d_{i-1}, d_{i-2}; \boldsymbol{\theta}_1, \boldsymbol{\theta}_2) = \frac{\prod_{i=3}^n l(d_{i-2}, d_{i-1}, d_i; \boldsymbol{\theta}_1, \boldsymbol{\theta}_2)}{\prod_{i=3}^{n-1} l(d_{i-1}, d_i; \boldsymbol{\theta}_1, \boldsymbol{\theta}_2)}, \quad (\text{A5})$$

and can therefore calculate the likelihood ratio using this likelihood formulation.

As described in Smith et al. (1997), the estimation of the model is similar to that for a first-order Markov process, but now also with respect to the newly introduced variable (trivariate problem). The likelihood formulation can then be written similarly to Sect. 3.2 and the fitting procedure is analogous to Sect. 4. However, because of the more complex likelihood structure, the fitting procedure is more costly than for the first-order Markov process.

The effect of choosing a second-order Markov process will be shown based on maximum temperature and the southern European region.

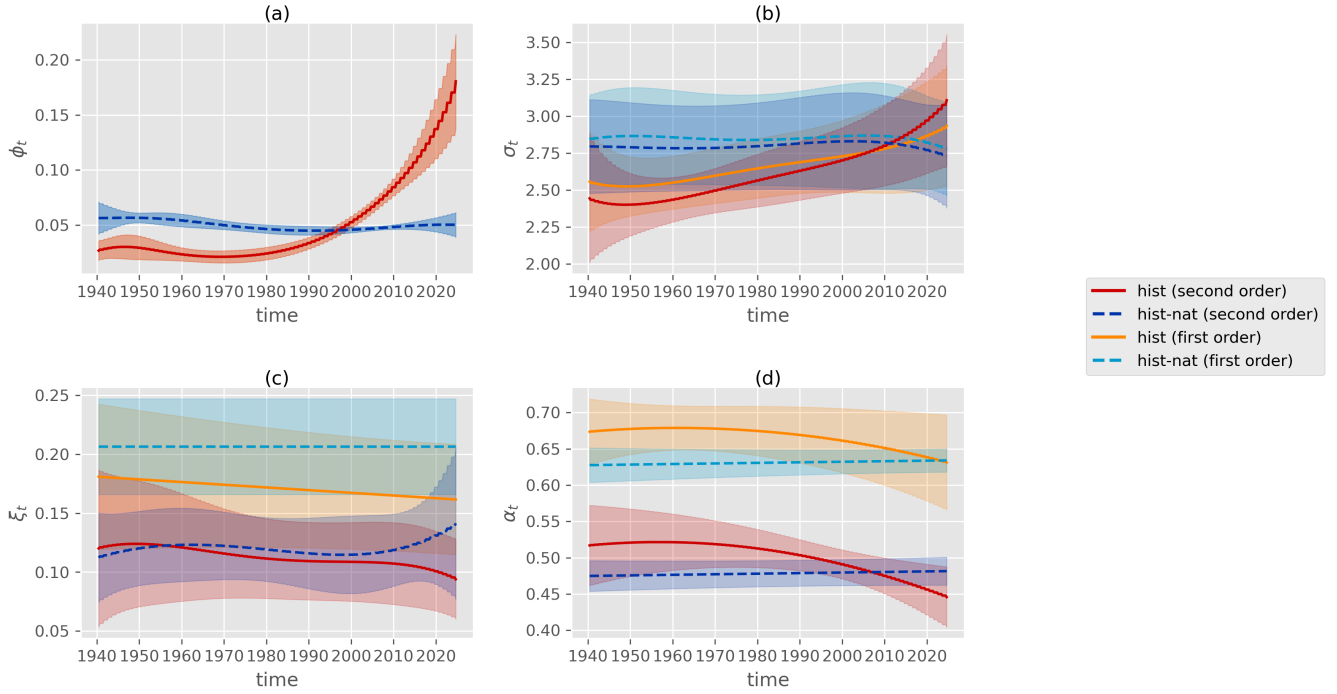


Figure A4. Same as Fig. 5 but now including the parameter estimates for the second order Markov process.

As can be seen in Fig. A4, the resulting and scale parameters are in a similar range for the first and second order Markov process. The shape parameter estimates are slightly higher for the second-order Markov process in both scenarios, indicating a tendency towards greater variability in the data. As expected, the main difference between using a first- and second-order Markov process lies in the dependence parameter. Using the second-order Markov process results in weaker dependence. A reason for this can be seen in the fact that for higher time lags, the variability of the atmosphere reduces the dependence.

When calculating the likelihood ratios for the second order Markov process model (Fig. A5), a tendency towards smaller values can be seen for the second-order Markov process model over a large number of years. This may indicate the presence of dependencies with a lag greater than one day, such that the resulting likelihoods differ due to the dependence assumption of the first-order Markov process.

In order to assess, if the second order Markov process gives a statistical improvement, the BIC (which is only one criterion pointed out by Smith et al. (1997) for the model comparison) is compared. For both scenarios and all climate models, the model of the second order Markov process gives an improvement in terms of the BIC.

A3 Parameter estimates for the northern and central European regions

The parameters for the northern and central European regions are estimated in a similar way to those for the southern European region, as shown in Sect. 5. For the model with a constant threshold, the estimated coefficients are quite similar across different

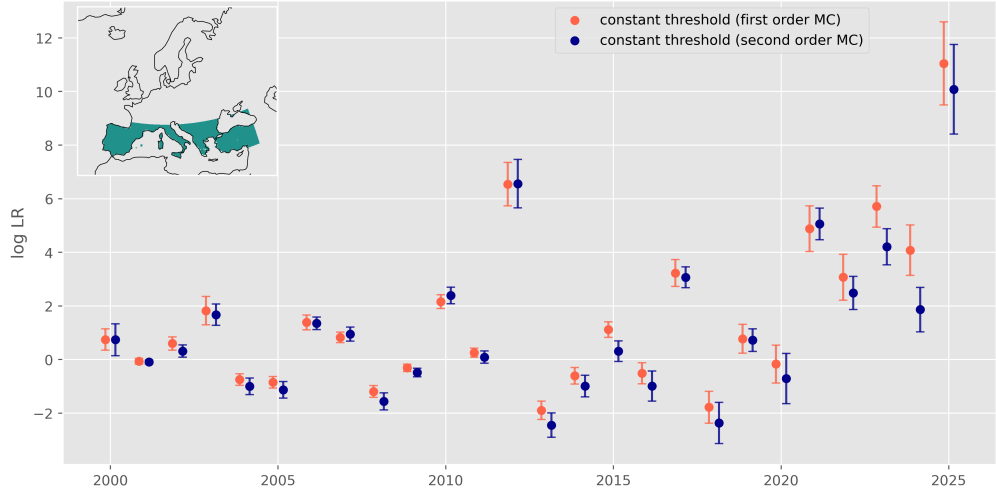


Figure A5. Effect of using a second order Markov process: the mean and \pm standard deviation of the likelihood ratios for the different climate models using a first and second order Markov process. For the sake of simplicity, we did not apply the random effect model to combine the probability ratios of the different models.

regions (Figs. A6 and A7), except for the shape parameter in the HIST scenario, where in the northern European region (Fig. A6) only the intercept is relevant for the different climate models, in contrast to the central and southern European region (Figs. A7 and 4).

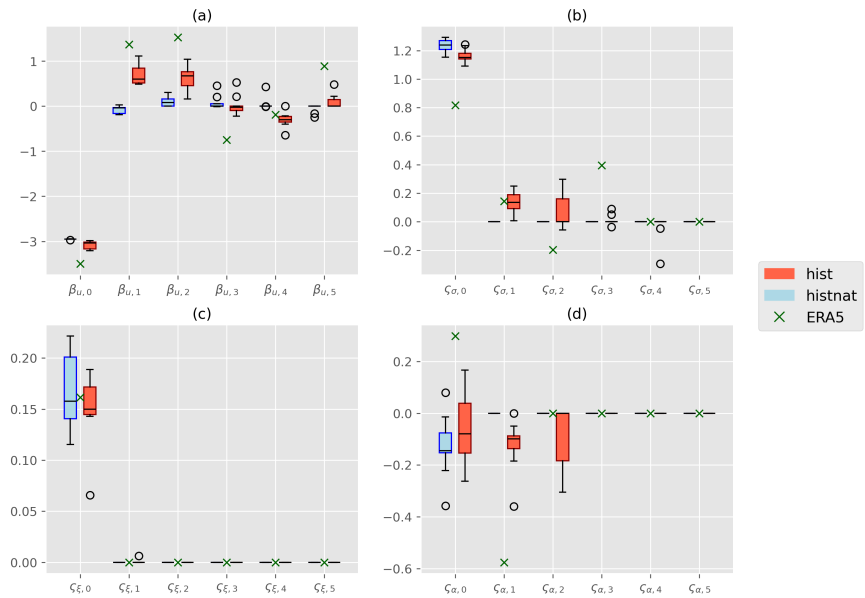


Figure A6. Same as Fig. 4 but for the northern European region.

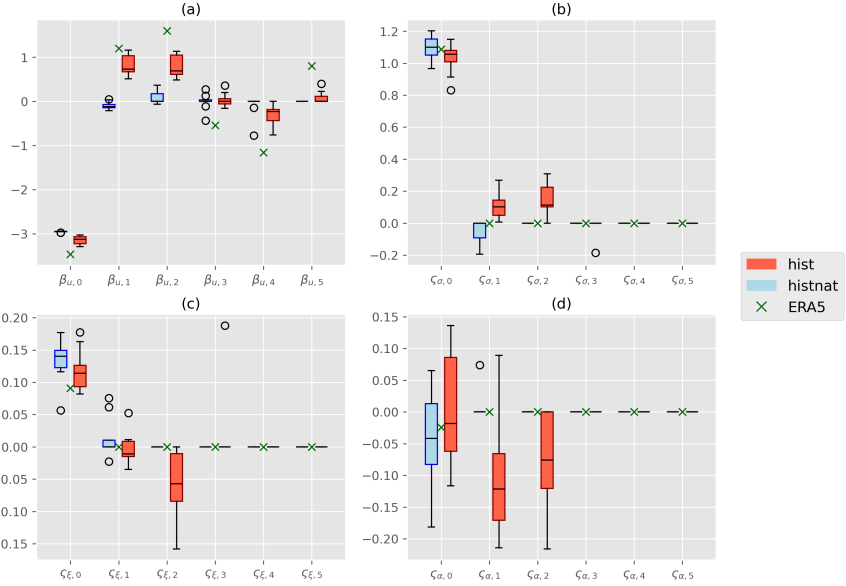


Figure A7. Same as Fig. 4 but for the central European region.

As in the model with a constant threshold, the coefficients show high similarity for the time-varying threshold model (Figs. A8 and A9). In the HIST scenario for the northern region, only coefficients up to degree two are relevant; in the other regions, however, higher-order coefficients also come into play.

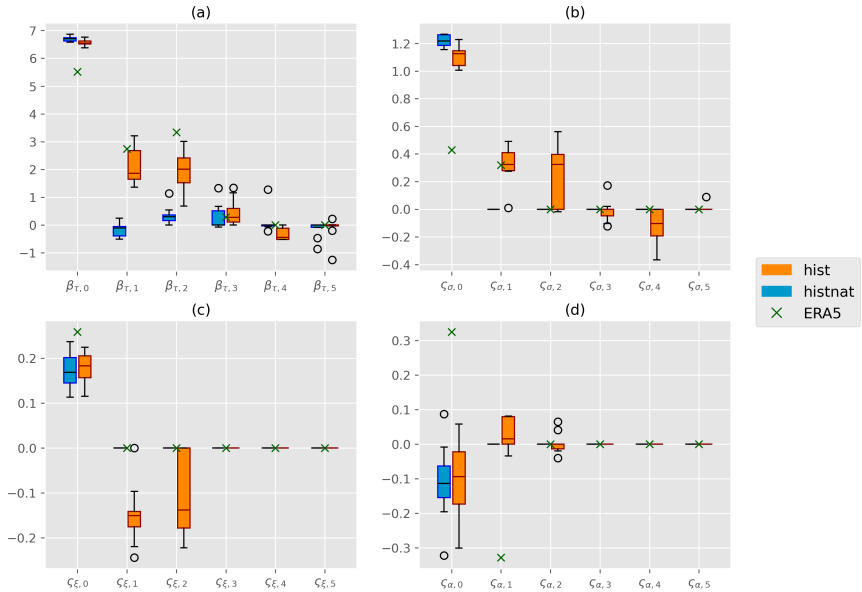


Figure A8. Same as Fig. 6 but for the northern European region.

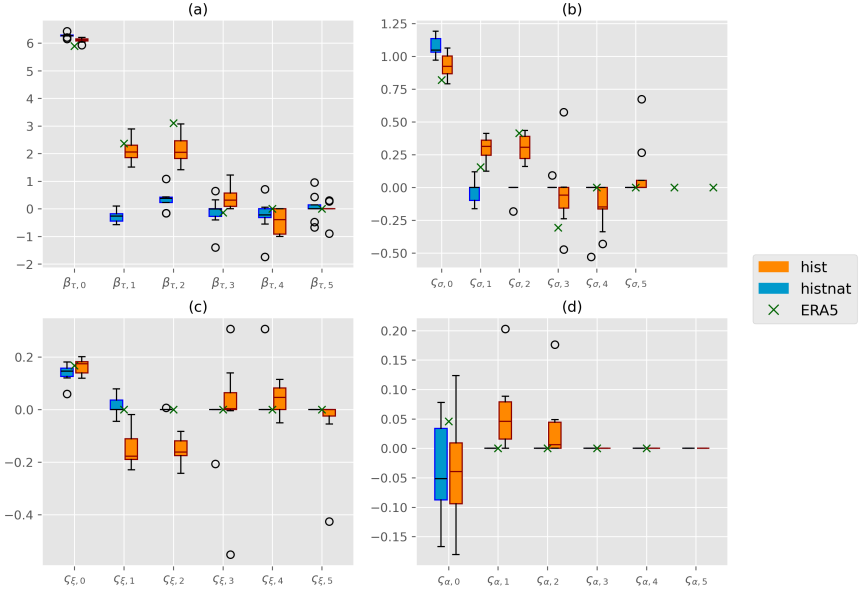


Figure A9. Same as Fig. 6 but for the central European region.

Code and data availability. This study used a selection of ERA5 and CMIP6 data stored at DKRZ. ERA5 is freely available via the Copernicus data store, CMIP6 data can be retrieved from the ESGF data nodes. An implementation of the extremal pattern index is available via the ExtrPatt R-package (<https://CRAN.R-project.org/package=ExtrPatt>). Python code for the non-stationary model fitting procedures is available from the first author upon request.

Author contributions. All of the authors contributed to developing the idea for this study (conceptualization). PF secured the funding of this work. PF and SB supervised the work. SvS provided support for the TPDM calculation. Data analysis and visualisation were performed by PM. PM also led the writing of the original draft. PF contributed to the original draft. All authors contributed to reviewing and editing the paper.

Competing interests. The authors declare that they have no conflict of interest.

Acknowledgements. This research was funded within the BMFTR project ClimXtreme II - Module B under grant number FKZ 01LP2323A. This work used resources of the Deutsches Klimarechenzentrum (DKRZ) granted by its Scientific Steering Committee (WLA) under project ID bm1159.

References

Barnes, C., Clarke, B., Rantanen, M., Skålevåg, A., Ødemark, K., Kjellström, E., Vahlberg, M., Singh, R., Otto, F., Zachariah, M., and et al.: Intense two-week heatwave in Fennoscandia hotter and more likely due to climate change, <https://doi.org/10.25560/122924>, 2025.

Beirlant, J., Goegebeur, Y., Segers, J., and Teugels, J.: *Statistics of Extremes: Theory and Applications*, Wiley, ISBN 0471976474, pagination: 522, 2004.

Chavez-Demoulin, V. and Davison, A.: Modelling Time Series Extremes, *REVSTAT-Statistical Journal*, 10, 109–133, <https://doi.org/10.57805/revstat.v10i1.113>, 2012.

Coles, S.: *An introduction to statistical modeling of extreme values*, Springer Series in Statistics, Springer-Verlag, London, ISBN 1-85233-459-2, 2001.

Cooley, D. and Thibaud, E.: Decompositions of dependence for high-dimensional extremes, *Biometrika*, 106, 587–604, <https://doi.org/10.1093/biomet/asz028>, 2019.

Copernicus Climate Change Service: Heatwaves contribute to the warmest June on record in western Europe, <https://climate.copernicus.eu/heatwaves-contribute-warmest-june-record-western-europe>, accessed on 08/10/2025., 2025.

Faranda, D., Guinaldo, T., Pastor, J. F., Alberti, T., and Khodayar, S.: Attribution of the 2025 Mediterranean Marine Heatwave to Climate Change Using Analogues, <https://hal.science/hal-05289765>, preprint, 2025.

Fawcett, L. and Walshaw, D.: Markov chain models for extreme wind speeds, *Environmetrics*, 17, 795–809, <https://doi.org/https://doi.org/10.1002/env.794>, 2006.

Friederichs, P.: Statistical downscaling of extreme precipitation events using extreme value theory, *Extremes*, 13, 109–132, <https://doi.org/10.1007/s10687-010-0107-5>, 2010.

Gillett, N. P., Shiogama, H., Funke, B., Hegerl, G., Knutti, R., Matthes, K., Santer, B. D., Stone, D., and Tebaldi, C.: The Detection and Attribution Model Intercomparison Project (DAMIP v1.0) contribution to CMIP6, *Geoscientific Model Development*, 9, 3685–3697, <https://doi.org/10.5194/gmd-9-3685-2016>, 2016.

Gulev, S., Thorne, P., Ahn, J., Dentener, F., Domingues, C., Gerland, S., Gong, D., Kaufman, D., Nnamchi, H., Quaas, J., Rivera, J., Sathyendranath, S., Smith, S., Trewin, B., von Schuckmann, K., and Vose, R.: Changing State of the Climate System, in: *Climate Change 2021: The Physical Science Basis. Contribution of Working Group I to the Sixth Assessment Report of the Intergovernmental Panel on Climate Change*, edited by Masson-Delmotte, V., Zhai, P., Pirani, A., Connors, S. L., Péan, C., Berger, S., Caud, N., Chen, Y., Goldfarb, L., Gomis, M. I., Huang, M., Leitzell, K., Lonnoy, E., Matthews, J. B. R., Maycock, T. K., Waterfield, T., Yelekçi, O., Yu, R., and Zhou, B., book section 2, Cambridge University Press, Cambridge, UK and New York, NY, USA, <https://doi.org/10.1017/9781009157896.004>, 2021.

Hannart, A. and Naveau, P.: Probabilities of Causation of Climate Changes, *Journal of Climate*, 31, 5507 – 5524, <https://doi.org/10.1175/JCLI-D-17-0304.1>, 2018.

Hannart, A., Pearl, J., Otto, F. E. L., Naveau, P., and Ghil, M.: Causal Counterfactual Theory for the Attribution of Weather and Climate-Related Events, *Bulletin of the American Meteorological Society*, 97, 99 – 110, <https://doi.org/10.1175/BAMS-D-14-00034.1>, 2016.

Hegerl, G. C., Karl, T. R., Allen, M., Bindoff, N. L., Gillett, N., Karoly, D., Zhang, X., and Zwiers, F.: Climate Change Detection and Attribution: Beyond Mean Temperature Signals, *Journal of Climate*, 19, 5058–5077, <http://www.jstor.org/stable/26259286>, 2006.

Hersbach, H., Bell, B., Berrisford, P., Hirahara, S., Horányi, A., Muñoz-Sabater, J., Nicolas, J., Peubey, C., Radu, R., Schepers, D., et al.: The ERA5 global reanalysis, *Quarterly Journal of the Royal Meteorological Society*, 146, 1999–2049, <https://doi.org/10.1002/qj.3803>, 2020.

Hulme, M.: Attributing weather extremes to 'climate change': A review, *Progress in Physical Geography: Earth and Environment*, 38, 499–511, <https://doi.org/10.1177/0309133314538644>, 2014.

Huser, R., Opitz, T., and Thibaud, E.: Max-infinitely divisible models and inference for spatial extremes, *Scandinavian Journal of Statistics*, 48, 321–348, <https://doi.org/https://doi.org/10.1111/sjos.12491>, 2021.

IEA: Global Energy Review: CO₂ Emissions in 2021 Global emissions rebound sharply to highest ever level, <https://www.iea.org/reports/global-energy-review-co2-emissions-in-2021-2>, accessed: 2025-07-30, 2021.

Iturbide, M., Gutiérrez, J. M., Alves, L. M., Bedia, J., Cerezo-Mota, R., Cimadevilla, E., Cofiño, A. S., Di Luca, A., Faria, S. H., Gorodetskaya, I. V., Hauser, M., Herrera, S., Hennessy, K., Hewitt, H. T., Jones, R. G., Krakovska, S., Manzanas, R., Martínez-Castro, D., Narisma, G. T., Nurhati, I. S., Pinto, I., Seneviratne, S. I., van den Hurk, B., and Vera, C. S.: An update of IPCC climate reference regions for subcontinental analysis of climate model data: definition and aggregated datasets, *Earth System Science Data*, 12, 2959–2970, <https://doi.org/10.5194/essd-12-2959-2020>, 2020.

Jeon, S., Paciorek, C. J., and Wehner, M. F.: Quantile-based bias correction and uncertainty quantification of extreme event attribution statements, *Weather and Climate Extremes*, 12, 24–32, <https://doi.org/10.1016/j.wace.2016.02.001>, 2016.

Jiang, Y., Cooley, D., and Wehner, M. F.: Principal Component Analysis for Extremes and Application to U.S. Precipitation, *Journal of Climate*, 33, 6441–6451, <https://doi.org/10.1175/JCLI-D-19-0413.1>, 2020.

Kass, R. E. and Raftery, A. E.: Bayes Factors, *Journal of the American Statistical Association*, 90, 773–795, <https://doi.org/10.1080/01621459.1995.10476572>, 1995.

Koenker, R.: Quantile regression, vol. 38 of *Econometric Society Monographs*, Cambridge University Press, 2005.

Koenker, R. and Machado, J. A. F.: Goodness of fit and related inference processes for quantile regression, *Journal of the American Statistical Association*, 94, 1296–1310, 1999.

Min, S.-K. and Hense, A.: A Bayesian Assessment of Climate Change Using Multimodel Ensembles. Part I: Global Mean Surface Temperature, *Journal of Climate*, 19, 3237 – 3256, <https://doi.org/10.1175/JCLI3784.1>, 2006.

Nelder, J. A. and Wedderburn, R. W.: Generalized linear models, *Journal of the Royal Statistical Society Series A: Statistics in Society*, 135, 370–384, 1972.

Otto, F. E. L., Barnes, C., Philip, S., Kew, S., van Oldenborgh, G. J., and Vautard, R.: Formally combining different lines of evidence in extreme-event attribution, *Advances in Statistical Climatology, Meteorology and Oceanography*, 10, 159–171, <https://doi.org/10.5194/ascmo-10-159-2024>, 2024.

Paciorek, C. J., Stone, D. A., and Wehner, M. F.: Quantifying statistical uncertainty in the attribution of human influence on severe weather, *Weather and Climate Extremes*, 20, 69–80, <https://doi.org/10.1016/j.wace.2018.01.002>, 2018.

Paule, R. C. and Mandel, J.: Consensus Values and Weighting Factors, *Journal of Research of the National Bureau of Standards (1977)*, 87, 377–385, <https://doi.org/10.6028/jres.087.022>, 1982.

Perkins-Kirkpatrick, S., Alexander, L., King, A., Kew, S., Philip, S., Barnes, C., Maraun, D., Stuart-Smith, R., Jézéquel, A., Bevacqua, E., Burgess, S., Fischer, E., Hegerl, G., Kimutai, J., Koren, G., Lawal, K., Min, S.-K., New, M., Odoulami, R., Patricola, C., Pinto, I., Ribes, A., Shaw, T., Thiery, W., Trewin, B., Vautard, R., Wehner, M., and Zscheischler, J.: Frontiers in attributing climate extremes and associated impacts, *Frontiers in Climate*, 6, <https://doi.org/10.3389/fclim.2024.1455023>, 2024.

Philip, S., Kew, S., van Oldenborgh, G. J., Otto, F., Vautard, R., van der Wiel, K., King, A., Lott, F., Arrighi, J., Singh, R., and van Aalst, M.: A protocol for probabilistic extreme event attribution analyses, *Advances in Statistical Climatology, Meteorology and Oceanography*, 6, 177–203, <https://doi.org/10.5194/ascmo-6-177-2020>, 2020.

Seabold, S. and Perktold, J.: statsmodels: Econometric and statistical modeling with python, in: 9th Python in Science Conference, 2010.

Seneviratne, S., Zhang, X., Adnan, M., Badi, W., Dereczynski, C., Di Luca, A., Ghosh, S., Iskandar, I., Kossin, J., Lewis, S., Otto, F., Pinto, I., Satoh, M., Vicente-Serrano, S., Wehner, M., and Zhou, B.: Weather and Climate Extreme Events in a Changing Climate, in: Climate Change 2021: The Physical Science Basis. Contribution of Working Group I to the Sixth Assessment Report of the Intergovernmental Panel on Climate Change, edited by Masson-Delmotte, V., Zhai, P., Pirani, A., Connors, S. L., Péan, C., Berger, S., Caud, N., Chen, Y., Goldfarb, L., Gomis, M. I., Huang, M., Leitzell, K., Lonnoy, E., Matthews, J. B. R., Maycock, T. K., Waterfield, T., Yelekçi, O., Yu, R., and Zhou, B., book section 11, pp. 1513–1765, Cambridge University Press, Cambridge, UK and New York, NY, USA, <https://doi.org/10.1017/9781009157896.013>, 2021.

Seong, M.-G., Min, S.-K., and Zhang, X.: A Bayesian Attribution Analysis of Extreme Temperature Changes at Global and Regional Scales, *Journal of Climate*, 35, 8189 – 8203, <https://doi.org/10.1175/JCLI-D-22-0104.1>, 2022.

Sippel, S., Mitchell, D., Black, M. T., Dittus, A. J., Harrington, L., Schaller, N., and Otto, F. E.: Combining large model ensembles with extreme value statistics to improve attribution statements of rare events, *Weather and Climate Extremes*, 9, 25–35, <https://doi.org/https://doi.org/10.1016/j.wace.2015.06.004>, the World Climate Research Program Grand Challenge on Extremes – WCRP-ICTP Summer School on Attribution and Prediction of Extreme Events, 2015.

Smith, R. L., Tawn, J. A., and Coles, S. G.: Markov chain models for threshold exceedances, *Biometrika*, 84, 249–268, <https://doi.org/10.1093/biomet/84.2.249>, 1997.

Stott, P. A., Stone, D. A., and Allen, M. R.: Human contribution to the European heatwave of 2003, *Nature*, 432, 610–614, <https://doi.org/10.1038/nature03089>, 2004.

Szemkus, S. and Friederichs, P.: Spatial patterns and indices for heat waves and droughts over Europe using a decomposition of extremal dependency, *Advances in Statistical Climatology, Meteorology and Oceanography*, 10, 29–49, <https://doi.org/10.5194/ascmo-10-29-2024>, 2024.

Wehner, M., Stone, D., Krishnan, H., AchutaRao, K., and Castillo, F.: The Deadly Combination of Heat and Humidity in India and Pakistan in Summer 2015, *Bulletin of the American Meteorological Society*, 97, S81 – S86, <https://doi.org/10.1175/BAMS-D-16-0145.1>, 2016.

Xoplaki, E., Ellsäßer, F., Grieger, J., Nissen, K. M., Pinto, J. G., Augenstein, M., Chen, T.-C., Feldmann, H., Friederichs, P., Gliksman, D., Goulier, L., Haustein, K., Heinke, J., Jach, L., Knutzen, F., Kollet, S., Luterbacher, J., Luther, N., Mohr, S., Mudersbach, C., Müller, C., Rousi, E., Simon, F., Suarez-Gutierrez, L., Szemkus, S., Vallejo-Bernal, S. M., Vlachopoulos, O., and Wolf, F.: Compound events in Germany in 2018: drivers and case studies, *Natural Hazards and Earth System Sciences*, 25, 541–564, <https://doi.org/10.5194/nhess-25-541-2025>, 2025.